



Published in final edited form as:

Nat Struct Mol Biol. 2022 July ; 29(7): 706–718. doi:10.1038/s41594-022-00792-w.

Architecture of the human erythrocyte ankyrin-1 complex

F. Vallese^{1,2}, K. Kim², L.Y. Yen², J.D. Johnston^{2,3}, A.J. Noble³, T. Call^{4,5}, O.B. Clarke^{1,2}

¹Department of Anesthesiology, Columbia University Irving Medical Center; New York, NY, 10032, USA.

²Department of Physiology and Cellular Biophysics, Columbia University; New York, NY, 10032, USA.

³Simons Electron Microscopy Center, New York Structural Biology Center; New York, NY, USA.

⁴Department of Biomedical Sciences, University of Padua; 35131 Padua, Italy.

⁵Padua Neuroscience Center (PNC), University of Padua; 35131 Padua, Italy.

Abstract

The stability and shape of the erythrocyte membrane is provided by the ankyrin-1 complex, but how it tethers the spectrin-actin cytoskeleton to the lipid bilayer and the nature of its association with the band 3 anion exchanger and the Rhesus glycoproteins remains unknown. Here we present structures of ankyrin-1 complexes purified from human erythrocytes. We reveal the architecture of a core complex of ankyrin-1, the Rhesus proteins RhAG and RhCE, the band 3 anion exchanger, protein 4.2, glycophorin A and glycophorin B. The distinct T-shaped conformation of membrane-bound ankyrin-1 facilitates recognition of RhCE and unexpectedly, the water channel aquaporin-1. Together, our results uncover the molecular details of ankyrin-1 association with the erythrocyte membrane, and illustrate the mechanism of ankyrin-mediated membrane protein clustering.

INTRODUCTION

An ordered lattice of spectrin and actin gives mechanical stability and shape to otherwise fragile cellular membranes. The periodic spectrin-actin cytoskeleton was first identified in erythrocytes¹, but has since been found in other cell types, including neurons². The spectrin-actin network is tethered to the membrane by giant, spring-like proteins known as ankyrins, which also serve the purpose of clustering diverse membrane proteins at specific sub-cellular locations.

Three ankyrin proteins are present in vertebrates: ankyrin-1 (ankyrin-R), ankyrin-2 (ankyrin-B) and ankyrin-3 (ankyrin-G). Ankyrins share a common domain arrangement, consisting of a highly conserved N-terminal membrane binding domain with 24 ankyrin repeats (AR1–

*Corresponding author. olibclarke@gmail.com.

Author contributions statement: F.V. with the assistance of L.Y.Y. performed protein preparation for structural analysis. F.V. and T.C. prepared membranes from human erythrocytes. F.V. screened and optimized sample vitrification, and generated cryo-EM data. Tomography data analysis was performed by J.D.J. and A.J.N. Single particle cryo-EM data analysis and model building was performed by O.B.C. The manuscript was written by O.B.C. and F.V. with input from T.C. Figures were prepared by K.K and F.V.

Competing interests' statement: The authors declare that they have no competing interests.

24), followed by a spectrin binding module (ZU5-ZU5-UPA; ZZU) and a death domain of unclear functional significance. The characteristic 24-repeat membrane binding domain of ankyrins has a groove on the inner concave surface that mediates recruitment of short peptides from target proteins, as well as mediating autoinhibition by regions of the MBD-ZZU linker and the C-terminal tail. Ankyrin-1 was first identified in erythrocytes³, where it mediates the attachment of the band 3 anion transport protein (AE1; SLC4A1) to spectrin⁴. It is also found in other tissues, including skeletal muscle and brain, where it has recently been shown to mediate clustering of Kv3.1b K⁺ channels in specific neuronal subtypes⁵. Ankyrin 2 and 3 play pivotal roles as dynamic adaptor platforms in cardiomyocytes and striated muscle cells⁶, and in neurons of the central⁷ and peripheral⁸ nervous systems, respectively.

In erythrocytes, ankyrin-1 attaches the cytoskeleton to the membrane via direct interaction with spectrin⁹, and additionally mediates clustering of integral membrane proteins, helping maintain the structure of the membrane and coordinating the spatial organization of transporters and channels involved in the regulation of cellular volume and cytosolic composition. Mutations in components of the erythrocyte ankyrin-1 complex are linked to an inherited anemia known as hereditary spherocytosis (HS), in which the characteristic biconcave disc shape of healthy erythrocytes is lost, resulting in small, fragile, spherical cells known as spherocytes¹⁰. Ankyrin and spectrin mutations are also associated with several other genetic diseases, including neurological and cardiac abnormalities¹¹. The erythrocyte ankyrin-1 complex is known to contain the band 3 chloride/bicarbonate exchanger, the adaptor molecule protein 4.2, the single transmembrane proteins glycoporphin A (GPA) and glycoporphin B (GPB), and the Rhesus proteins RhAG and RhCE¹². Other proteins that are believed to associate with the ankyrin-1 complex include GLUT1¹³, LW and CD-47¹⁴. However, the stoichiometry and architecture of the complex remains unknown, making it close to impossible to reconstitute recombinantly.

Here, we purified the ankyrin-1 complex from human erythrocytes, and captured a series of high-resolution structures by single particle cryo-electron microscopy (cryo-EM), complemented by a sub-tomogram average of the complex in the context of native erythrocyte membrane fragments. These revealed its architecture and composition, shedding light on the mechanism of membrane protein recruitment by ankyrin and protein 4.2, and identifying aquaporin-1 as an unanticipated component of the ankyrin-1 complex.

RESULTS

Structure determination of the ankyrin-1 complex.

The ankyrin-1 complex was purified from digitonin-solubilized human erythrocyte ghost membranes by density gradient centrifugation, followed by size exclusion chromatography (Fig. 1a, Supplementary Fig. 1a,b and MovieS1). The final sample contained a major 1.2 MDa species as assessed by mass photometry¹⁵(Supplementary Fig. 1c). The presence of major components of the erythrocyte ankyrin-1 complex, including ankyrin-1, band 3, protein 4.2, GPA and RhAG was assessed by SDS-PAGE and confirmed by mass spectrometry analysis (Supplementary Table 1).

Cryo-EM analysis of the purified sample revealed both a mixture of ankyrin-1 containing complexes, as well as smaller complexes of free band 3 with GPA (Extended Data Fig. 1a,b and Supplementary Fig. 1d).

After repicking using a Topaz model trained on the smaller complexes¹⁶, *Ab initio* reconstruction and refinement of the band 3-GPA class gave a C1 reconstruction at 2.8 Å. Both protomers were in the outward open state, and the transmembrane domains exhibit apparent C2 symmetry. Refinement gave a 2.3 Å reconstruction with C2 symmetry applied, allowing us to build a complete atomic model of the band 3-GPA complex (Extended Data Fig. 1c).

Refinement of all 710k ankyrin-1-containing particles against an *ab initio* reference yielded a 2.4 Å consensus reconstruction (Extended Data Fig. 2). Well-ordered density is observed for the Rh heterotrimer, ankyrin-1, protein 4.2, and the cytoplasmic domains of a single band 3 dimer (denoted subsequently as Band 3-I). Masked refinement and in some cases focused 3D-variability analysis was used to improve the density quality for each component (Extended Data Fig. 3).

Sub-classification of the ankyrin complexes revealed six distinct classes with variable composition (Extended Data Fig. 4a). The core architecture is conserved in all six classes, but with elaborations. Class 1 had a larger micelle than observed in the consensus refinement, accommodating two additional band 3 dimers (denoted Band 3-II and Band 3-III) that interact directly with ankyrin. 2D classes of Class 1 resemble complexes identified in native membrane vesicles using cryo-electron tomography (Fig. 1d, Extended Data Fig. 5, Supplementary Fig. 2 and Movie S2, S3). Classes 2 and 5 had an additional component present that proved to be an aquaporin 1 (AQP1) tetramer. Class 4 has an overall architecture similar to Class 1, but with a somewhat different orientation of the Band 3-I transmembrane region, and the presence of an unknown membrane protein.

While the cytoplasmic domains of Band 3-I were well ordered in the consensus refinement, the transmembrane domains were very poorly resolved, which we rectified using the following classification scheme. After local refinement gave a poor quality 3.8 Å map, 3D-variability analysis was performed in cryoSPARC using a mask around the Band 3-I TM. Clustering with a single mode corresponding to an order-disorder transition of the transmembrane region allowed identification of a 226k particle subset for which local refinement gave a 2.8 Å map with excellent density quality, and a well-resolved interface with protein 4.2 (Extended Data Fig. 6). A similar approach was applied to improve the density of Band 3-II and Band 3-III starting from Class 1, resulting in 3.3 and 3.0 Å local refinements, respectively.

By applying this clustering approach to Class 2, a particle subset was identified with improved AQP1 density, resulting in a 3.0 Å C1 map that facilitated unambiguous fitting of the AQP1 crystal structure, and identification of the regions of AQP1 that interact with ankyrin-1 and protein 4.2. Application of local C4 symmetry yielded a 2.4 Å map (Movie S4).

We have used the reconstructions described above to build atomic models for Class 1a (Fig. 1b), which we believe represents an intact complex, and Class 2, in which the interaction with AQP1 is best defined, as well as for the consensus refinement of all classes, which had the best resolved density at the core of the complex. AQP1 is present in classes 2 and 5. The remaining classes may represent genuine diversity in the composition of complexes present in the membrane, or partial dissociation of a single native complex (Extended Data Fig. 4a). The association of AQP1 in classes 2 and 5 appears compatible with the arrangement of band 3 dimers in Class 1, despite a substantial rigid body rearrangement of the transmembrane domains of Band3-I in the presence of AQP1 (Extended Data Fig. 4b). We therefore assess that *in vivo*, the three band 3 dimers identified here, as well as AQP1, are likely to be part of the same complex. This conclusion is supported by analysis of tomograms obtained from vesicles generated by extrusion of native erythrocyte membranes. The appearance of particles in the tomograms is very similar to the 2D classes obtained by single particle analysis (Movie S2), and sub-tomogram averaging of particles extracted from the tomograms identifies a class with near identical architecture to Class 1/1a (Fig. 1d, Supp. Fig. 2a,b, Movie S3). The absence of CD-47 and LW from the complex may indicate that they are loosely associated, and lost during digitonin extraction, or that they are associated with a distinct complex that we have not isolated.

Architecture of the human erythrocyte ankyrin-1 complex.

The architecture of Class 1a is presented in Figure 1 and Movie S1. The membrane-embedded core of the complex is formed by the (RhAG)₂(RhCE) heterotrimer. Ankyrin binds to the N- and C-termini of RhCE, via the first five ankyrin repeats (AR1–5), which are oriented parallel to the membrane. The subsequent ankyrin repeats (AR6–24) emerge perpendicularly downwards from a T-interface with AR1–5, and gradually recurve to run almost parallel to the membrane.

Protein 4.2 is oriented vertically, such that the myristoylated N-terminus contacts the membrane, with one flat surface bound to AR1 and AR6–13 of ankyrin, while the distal face recruits band 3.

Three band 3-GPA dimers (Band 3-I, Band 3-II and Band 3-III) form part of the complex. Band 3-I binds to the distal face of protein 4.2 via the band 3 cytoplasmic domain and N-terminal peptide. Band 3-II and Band 3-III, by contrast, both interact directly with ankyrin. Band 3-II interacts with the outer face of AR17–19 via the cytoplasmic domain, while the cytoplasmic domain of Band 3-III binds to the outer face of AR21–24, and the Band 3-III N-terminal peptide runs back along the inner groove of ankyrin.

Membrane association and target recruitment by ankyrin-1.

We observe simultaneous engagement of the ankyrin-1 membrane binding domain with multiple targets (Fig. 2a) that fall into three distinct categories: membrane embedded (RhCE & AQP1), extramembrane (cytosolic domains of band 3) and peripheral adaptors (protein 4.2). The integral membrane targets, RhCE and AQP1, both interact with the peptide binding groove of AR1–5; the adaptor (protein 4.2) interacts with the exterior surface of AR1–13; and the two extramembrane targets (Band 3-II & Band 3-III) interact predominantly with the

exterior surface of AR17–24, supplemented in the case of Band 3-III by interactions of the N-terminus with the peptide binding groove of AR6–10.

The Rh heterotrimer forms the primary membrane attachment site for ankyrin-1, mediated via an interaction between the N- and C-termini of RhCE and the first five repeats of ankyrin-1 (Fig. 2d). The structure of ankyrin-1 in the complex (Extended Data Fig. 7a) adopts a T-shaped arrangement in which AR1–5 are orthogonal to AR6–24, with the peptide binding groove of AR1–5 oriented towards the membrane. This is distinct from the extended conformation observed for ankyrin-2 bound to autoinhibitory motifs¹⁷ (Extended Data Fig. 7b). Comparison of the structures of AR1–9 of ankyrin-2 bound to a peptide from the NaV1.2 channel¹⁸, an ankyrin membrane target, with structures bound to the autoinhibitory peptide, shows substantial flexibility at the AR5–6 interface (Extended Data Fig. 7b,c), albeit not quite to the extent seen here in ankyrin-1. A sequence alignment of the 24 repeats of ankyrin-1 (Extended Data Fig. 7e) shows that, while AR5 and AR6 are highly conserved when compared to the equivalent regions of ankyrin-2 and ankyrin-3 (Extended Data Fig. 7f), they are the most divergent of the ankyrin repeats when compared with the other repeats in the ankyrin-1 MBD. The rearrangement of the AR1–5 module orients the canonical protein binding groove to directly face the membrane, in order to bind the membrane-embedded targets RhCE (in all classes) and AQP1 (Classes 2 & 5) (Extended Data Fig. 4a).

Protein 4.2 forms multiple sites of attachment to ankyrin-1, all of which are outside the canonical peptide binding groove (Fig. 2c). Protein 4.2 acts as an adaptor molecule and a stabilizer for ankyrin, with the outer face of protein 4.2 forming the attachment site for Band 3-I (Fig. 2b). Interaction of domain 1 of protein 4.2 with the exposed “edge” of AR1 appears to further stabilize the T-shaped conformation of the ankyrin-1 membrane binding domain (Fig. 2c).

In Class 1, Band 3-II and Band 3-III directly bind to ankyrin, interacting with repeats 17–19 & 21–24 respectively (Fig. 2e,f). The N-terminus of Band 3-III runs back along the inner ankyrin groove, with residues 2–24 forming an ordered interaction with AR6–10 and the AR5–6 linker (Extended Data Fig. 8a,b,c and Movie S5). This peptide is reversed when compared to the binding mode of ankyrin autoinhibitory motifs (Extended Data Fig. 8d,e,f), but in the same direction as the NaV 1.2 N-terminal peptide bound to ankyrin-2¹⁸ (Extended Data Fig. 7d). The orientation of the Band 3-I cytoplasmic domains is inverted with respect to the membrane when compared with Band 3-II & Band 3-III, which are both directly bound by ankyrin (Extended Data Fig. 9a). Interacting surfaces of band 3 cytoplasmic domains are distinct and non-overlapping (Extended Data Fig. 9b).

Structure of protein 4.2 and interactions with band 3.

The 2.2 Å structure of protein 4.2 is solved here in the context of the ankyrin-1 complex (Fig. 3a,b). As previously suggested^{19,20}, the fold of protein 4.2, is very similar to that of the closed conformation of tissue transglutaminase (TG2). The central papain-like domain (domain 2) is surrounded by three Ig-like domains (domains 1, 3 & 4). The N-terminal glycine of protein 4.2 is known to be myristoylated²¹, and here we see that the N-terminus directly contacts the membrane. The inner face of protein 4.2 interacts with ankyrin-1,

while the outer face forms the primary binding site for Band 3-I (Fig. 3c,d). The Band 3-I binding mode shares some broad similarities with the binding mode of Band 3-II to ankyrin (Extended Data Fig. 9b), insofar as it involves recognition of a 3D epitope via an extensive interface, and is augmented by interaction of the free N-terminus of band 3 with a peptide recognition groove. The interaction with Band 3-I is mediated by interactions with D4 & D1 of protein 4.2 (Fig. 2b), and the N-terminus of Band 3-I is nestled in a groove formed by D1, D2 & D4. In Class 2, D1 of protein 4.2 also appears to be forming interactions with AQP1. D1 is also forming an interface with loops near the transmembrane dimerization interface of Band 3-I, in a region that also forms cytoplasmic-TM contacts in Band 3-II (Extended Data Fig. 9c).

Aquaporin is a component of the ankyrin-1 complex.

A final resolution of 2.5 Å after local refinement with C4 symmetry allows unambiguous fitting of the crystal structure of AQP1 to the density map (Fig. 4a). Clear density is seen for waters in the pore (Extended Data Fig. 10a), as well as a lipid like density directly attached to Cys-87, which we have assigned as a palmitoylation site (Fig. 4b). AQP1 is located at the mutual interface of Band 3-I, protein 4.2, and AR1-2 (Fig. 4c,d). The interaction appears to be largely mediated by interactions of the N-terminus of AQP1 with AR1-2, and interactions of the C-terminus of AQP1 with domain 1 of protein 4.2 (Fig. 4e). In addition, strong, unmodeled density is present in the cleft between AQP1 and RhCE, underneath a patch of positively charged residues contributed by ankyrin, suggesting the possibility of a lipid-mediated interaction with ankyrin-1 and the Rh heterotrimer (Extended Data Fig. 10b). The position of the Band 3-I transmembrane domains is altered substantially in the presence of AQP1 as compared to Class 1 or the consensus refinement, with a translation of ~16 Å putting it in close contact with AQP1, and breaking the interaction of Band3-I with protein 4.2.

Structure and composition of the Rh channel.

In the structure of the erythrocyte ankyrin-1 complex presented here, we have resolved the structure of the Rh heterotrimer at 2.2 Å, (Fig. 5a,b and Extended Data Fig. 3) revealing that it contains two molecules of RhAG and one of RhCE (Extended Data Fig. 10c,d), with the N- and C- termini of RhCE interacting with ankyrin-1 (Fig. 2d). RhAG also helps stabilize this interaction, as the RhCE termini pack on top of the adjacent RhAG protomers. Several cholesterol and digitonin molecules are bound to the transmembrane regions of both RhAG and RhCE on both leaflets of the membrane (Fig. 5a,b). The pore of RhAG shows the expected twin-histidine motif in the center of the pore (Extended Data Fig. 10e), with a hydrogen bonded network of water molecules similar to that seen in the structures of AmtB and RhCG. The pore of RhCE is open to both the cytosolic and extracellular sides, with only a short central occlusion (Fig. 5c and Extended Data Fig. 10f), raising the possibility that RhCE may have a role in membrane transport. The density for RhCE is also weaker than for RhAG, despite the fact that RhCE is the subunit that directly engages with ankyrin. This weaker density (and correlated higher atomic B-factors) may indicate flexibility, possibly consistent with an unresolved conformational change corresponding to pore opening (Fig. 5c). Inspection of the map at sites of RhCE/D variation strongly suggests that RhCE is

predominantly incorporated (Extended Data Fig. 10h), consistent with previous findings suggesting preferential association of RhCE with the band 3 complex²².

Local refinement of the Rh trimer in Class 1 revealed an additional transmembrane helix bound to RhAG1 in a groove formed by TM1, TM3 and TM5, with the C-terminal end extending towards Band 3-III. Further classification, using a mask around the Rh trimer and Band 3-III, identified a class of 22k particles in which this density was much better defined, allowing assignment as glycophorin B (residues 59–91) (Fig. 5d), however given the sequence similarity with GPA in the TM region some ambiguity remains in this assignment. The N-terminal half of the helix forms the best-defined interactions with RhAG1, with the sidechain of Met71 buried in a hydrophobic pocket formed by Trp93, Ile146, Met16, Leu19 and Leu12 (Fig. 5e). The C-terminal end of the GPB helix (residues 86–91) appears to be forming a weak interaction with the N-terminal juxtamembrane helix of Band 3-III.

Structure of the band 3 dimer complexed with glycophorin A.

In the structure of the free band 3 dimer (Fig. 6a,b), a GPA monomer is bound at each end of the band 3 dimer, with the GPA transmembrane helix interacting primarily with TM4 of band 3, and the extracellular N-terminal peptide interacting with the TM7–8 loop (Fig. 6c). A tightly bound cholesterol molecule is located near the extracellular side, wedged between the transmembrane helix of GPA and TM8 of band 3 (Fig. 6c). A prominent lipid headgroup density is located at the intracellular dimer interface of band 3, where it binds to a patch of positively charged residues. Based on the distinctive shape of the density, and previous biochemical data showing enrichment of phosphoinositides in purified band 3²³ we have assigned this density as PI(4,5)P₂ (Fig. 6d, Movie S6). This density is also observed in classes of the intact ankyrin complex, where it is located very close to the interface of Band 3-I with protein 4.2 (Fig. 6e,f).

DISCUSSION

Ankyrins form part of an intricate sub-membrane lattice that provides mechanical stability, shape, and local functional organization to cellular membranes in many cell types including erythrocytes and neurons. In erythrocytes, ankyrin-1 forms the nucleus of a macrocomplex which acts to tether spectrin to the membrane³ and organizes several highly abundant membrane proteins involved in gas exchange, pH regulation, and control of cellular volume²⁴ (Supplementary Fig. 3). Mutations in elements of this complex lead to defects in erythrocyte size, shape and stability¹⁰. However, the architecture and composition of the complex, as well as the mechanism of ankyrin-1 recruitment to the membrane, have so far remained unresolved. Here, we used single-particle cryo-EM to determine structures of an erythrocyte ankyrin-1 complex that includes both the RhAG/CE heterotrimer and band 3. We provide a mechanistic hypothesis for ankyrin recruitment and autoinhibition, showing how ankyrin-1 can recruit three band 3 dimers at distinct sites, clarifying the role of protein 4.2, and identifying aquaporin-1 as an unanticipated component of the ankyrin-1 complex.

Membrane-bound ankyrin-1 adopts a T-shaped conformation.

The discontinuous, T-shaped conformation of ankyrin-1 we observe in the membrane bound state is strongly suggestive of a rearrangement upon membrane binding, which we propose is linked to the mechanistic basis of both ankyrin membrane association and autoinhibition. The only prior structure of a full-length ankyrin membrane binding domain is that of ankyrin-2 fused to the autoinhibitory C-terminal tail of ankyrin-1¹⁷, which binds in a continuous groove that traverses the entire length of the molecule. Constructs lacking the autoinhibitory peptide failed to crystallize, likely because they were too conformationally heterogeneous. In contrast, in our structure (Fig. 1a), the ankyrin-1 repeats AR1–5 are oriented parallel to the membrane, and orthogonal to the downstream ankyrin repeats. While there is no autoinhibited structure of ankyrin-1 available, the membrane binding domain and the AR5–6 region in particular are highly conserved in all three ankyrin proteins, suggesting that this is unlikely to be an isoform-specific difference. In the ankyrin-2 AR1–24 structure, the autoinhibitory peptide occupies a groove that crosses the AR5–6 boundary, stabilizing them in the “extended” state. By contrast, in our structure, the N-terminal peptide of Band 3-III occupies this same groove, but ends at the AR5–6 interface, with the very N-terminal 11 residues, including the Syk phosphorylation site Y8, appearing to stabilize it in the T-shaped, “hammerhead” configuration (Extended Data Fig. 8d and Movie S5). Deletion of these 11 residues in the band 3 Neapolis mutant causes a severe hemolytic anemia, without compromising insertion into the membrane²⁵. Phosphorylation of Y8 also causes alterations in erythrocyte size and shape²⁶, consistent with a role for this segment in stabilizing the membrane-associated configuration of ankyrin. We hypothesize that the Band 3-III N-terminal peptide displaces the autoinhibitory motif from the inner groove of ankyrin, freeing AR1–5 to adopt the membrane-associated configuration, and leaving the AR1–5 groove unoccupied, facilitating recognition of RhCE and AQP1. Band 3-III is also the band 3 dimer which has a GPB-mediated interaction with RhAG1 in Class 1a. It is possible that pre-association of RhAG/CE and Band 3 via GPB could facilitate recruitment of ankyrin-1, with band 3 first displacing the autoinhibition motif, and then AR1–5 binding to RhCE (Supplementary Fig. 4). Binding to protein 4.2 further stabilizes the T-shaped configuration of ankyrin, resulting in the core complex. In this model, the autoinhibited state is not competent to bind to the membrane not only because the inner groove is occupied, but also because AR1–5 are unable to access membrane embedded targets in the “extended” state.

Band 3 clustering is mediated by ankyrin-1 and protein 4.2.

The ankyrin-1 complex structure reveals four distinct sites of target recruitment (Fig. 2a). We term these sites the juxtamembrane (AR1–5 binding of RhCE and AQP1), the adaptor-mediated (protein 4.2 recruitment of Band3-I), the central (AR16–18 binding of Band3-II) and the distal site (Band-3-III binding, including interactions of N-terminal peptide). The observation that band 3 associates directly with ankyrin at the distal and central sites is consistent with studies of AR13–24 binding to the cytoplasmic domain of band 3, which identified a high affinity and a low affinity site²⁷. Band 3 has variously been characterized as binding to ankyrin as a bona fide tetramer, or a “pseudotetramer”, in which ankyrin links two band 3 dimers. Our structure is consistent with the latter model. The central site is broadly in agreement with the EPR-based structural model of Kim et al.²⁸, as well as studies

showing the importance of loops 175–185 and 63–73 of the band 3 cytoplasmic domain for interaction with ankyrin²⁹. In contrast, the distal site uses an entirely different interface on both ankyrin and the band 3 cytoplasmic domain, and is further stabilized by interactions of the N-terminal peptide of band 3 with the peptide binding groove of ankyrin.

Monomeric glycophorin A binds to the band 3 dimer.

One GPA monomer binds to each band 3 protomer, with the GPA transmembrane helix packing with TM3 and TM4 of band 3, and the extracellular N-terminal extension interacting with the TM7–8 loop, which includes E658, the critical residue for formation of the Wright blood group antigen³⁰. H85 of GPA appears to be forming a salt bridge with E658, likely representing the interaction that is variously present and absent in the different Wright blood types. This had previously been proposed to originate from a salt bridge with R61 of GPA³⁰, which is disordered in our structure. A cholesterol-mediated interaction with TM8 of band 3 is also observed, consistent with the known importance of TM8 in the band 3-GPA interaction³¹. Only monomeric GPA is observed binding to band 3, despite the known propensity of GPA to dimerize. This is consistent with studies showing that mutations which inhibit GPA dimerization do not inhibit band 3 dependent effects of GPA³², but still leaves a puzzle: why does the GPA dimer not interact with band 3? Structural alignment of the crystal structure of the GPA dimer³³ with band 3-bound GPA shows that the second molecule of GPA would have to be embedded entirely within the membrane, in an almost horizontal orientation, which is highly energetically unfavorable. We speculate that in the membrane, GPA exists in a monomer-dimer equilibrium, and band 3 selectively binds monomeric GPA. In the context of the Class 1 model of the ankyrin-1 complex, the GPA molecules bound to Band 3-II and Band 3-III are in close proximity, though we cannot be certain they are interacting. The possibility of GPA mediating end-to-end attachment of two band 3 dimers would be consistent with both previous molecular dynamics simulations of band 3 in the presence of modeled GPA³⁴, as well as the known propensity of detergent-solubilized band 3 purified from erythrocytes to form “tetramers” in solution³⁵.

Protein 4.2 facilitates recruitment of Band 3-I and AQP1.

The structure of the ankyrin-1 complex also establishes a role for protein 4.2, a highly abundant component of the erythrocyte. Protein 4.2 is known to interact with both band 3 and ankyrin³⁶, but the implication of these interactions was unclear. We observe that protein 4.2 plays a role as an adaptor, stabilizing the interaction of ankyrin with the membrane and facilitating recruitment of an additional dimer of the band 3 anion exchanger (Band 3-I) via interactions with both the cytoplasmic and TM regions, the latter of which appears to be at least partially mediated by a PIP₂ lipid bound at the band 3 transmembrane dimer interface. Furthermore, protein 4.2 appears to play an additional role in facilitating the recruitment of AQP1, the C-terminus of which directly interacts with domain 1 of protein 4.2.

Aquaporin-1 is a component of the ankyrin-1 complex.

The identification of aquaporin-1 as a component of the ankyrin-1 complex (Fig. 4) was an unexpected finding, although consistent with FRET measurements indicating that AQP1 is located within 8nm of band 3 dimers³⁷. The observation that AQP1 expression is decreased, and glycosylation pattern altered in both murine and human erythrocytes lacking band 3²⁴ is

also compatible with a role for AQP1 in the ankyrin-1 complex. It has been proposed that the cluster of membrane proteins that ankyrin-1 organizes in the red blood cell membrane forms a “CO₂ metabolon”³⁸, linking facilitated diffusion of CO₂ across the membrane, anion exchange of Cl⁻/HCO₃⁻ via band 3, and interconversion of dissolved CO₂ and carbonic acid in the cytosol via carbonic anhydrase, which binds to the C-terminal tail of band 3³⁹ and catalyzes conversion of CO₂ and H₂O to HCO₃⁻ and H⁺. A role for AQP1 in the CO₂-metabolon would be consistent with the known capacity of AQP1 to conduct both CO₂ and H₂O⁴⁰, both of which are substrates for carbonic anhydrase. RhAG may also participate indirectly in this process, by allowing facilitated diffusion of NH₃ and consequent modulation of [H⁺], via the equilibrium of NH₃ + H⁺ and NH₄⁺.

RhCE recruits ankyrin-1 to the membrane.

The heterotrimeric Rh ammonia channel plays an important role in ammonium homeostasis in the blood⁴¹, and in maintaining the stability of the red blood cell membrane¹². Humans express five Rh family proteins – RhAG, RhCE and RhD in erythrocytes, and RhBG and RhCG in the kidney epithelium. The structure of the RhCG homotrimer⁴² showed that the eukaryotic Rh family shares a great deal of similarity to the bacterial AmtB family of ammonium transporters, including a conserved twin histidine motif in the central pore. It has been suggested that RhAG mediates ammonia or possibly carbon dioxide transport^{43,44} across the erythrocyte membrane⁴⁵. The functional role of RhCE and RhD in the structure and function of the red blood cell membrane has been much debated, as has the stoichiometry of the heterotrimeric Rh complex. The 2.2 Å resolution structure of the (RhAG)₂RhCE heterotrimer (Fig. 5a,b) in the context of the ankyrin-1 complex resolves the stoichiometry question, and suggests that the primary role of RhCE might be as a recruitment site for ankyrin-1, via binding of the N and C-termini to AR1–5 of ankyrin-1. Other putative roles for RhCE remain speculative. It has been proposed, based on homology modeling⁴⁶ and the absence in RhCE/D of the characteristic twin histidine motif, that RhCE and RhD lack a membrane transport function completely. Our work, while not conclusively demonstrating that RhCE retains a transport function, shows that RhCE has a pore which extends almost completely across the membrane, impeded by only by a small cluster of hydrophobic residues, and which appears more dynamic than RhAG. We therefore suggest that the possibility of an auxiliary transport function for RhCE in the erythrocyte membrane may be worth investigating.

Concluding remarks.

In summary, we have reported the structure of an erythrocyte ankyrin-1 complex, purified from human erythrocytes. We have structurally characterized two direct binding sites for the band 3 anion exchanger on ankyrin-1, as well as one band 3 binding site mediated by protein 4.2, identified aquaporin-1 as a component of the complex, determined the stoichiometry of the heterotrimeric Rhesus ammonia channel, and identified RhCE as the ankyrin-1 binding subunit of the Rhesus channel. Taken together these findings offer insights into the molecular architecture of the red blood cell membrane, and show how ankyrins can facilitate the simultaneous recruitment of multiple classes of membrane proteins, to enable functional organization of membrane transport processes.

Methods:

Preparation of erythrocyte ghost membranes—Ghost membranes were prepared as described in Niggli et al.⁴⁷. Briefly, red blood cells from healthy blood donors were provided by the Transfusion Centre of the Hospital of Padua (Italy). Samples were obtained from voluntary and informed blood donation for transfusions. Erythrocytes from fresh human blood samples were washed twice in 5 volumes of 130 mM KCl, 10 mM Tris-HCl, pH 7.4. The cells were hemolyzed in 5 volumes of 1 mM EDTA, 10 mM Tris-HCl, pH 7.4, and centrifuged at $18,000 \times g$ for 10 min. The ghost membranes were then washed five times in the hemolysis buffer, and four additional times in 10 mM HEPES, pH 7.4. The hemoglobin-free ghost membranes were finally resuspended in 130 mM NaCl, 20 mM HEPES, pH 7.4, 0.5 mM MgCl₂, 0.05 mM CaCl₂, 2 mM DTT, and stored at -80°C .

Purification of the erythrocyte ankyrin-1 complex—The general purification workflow is presented in Supplementary Fig 1. Ghost membranes were solubilized at a protein concentration of 4 mg/ml in 130 mM KCl, 10 mM HEPES, pH 7.4, protease inhibitor tablet (cOmplete™, EDTA-free Protease Inhibitor Cocktail, Millipore Sigma), 1% (w/v) digitonin (Carbosynth), 1 mM ATP, 1 mM MgCl₂, 1 mM PMSF, at 4°C for 1 hour. Insolubilized material was removed by centrifugation at $26,000 \times g$ for 30 min. The supernatant was applied to a PD10 column (to reduce the detergent concentration) equilibrated with 0.05% (w/v) digitonin, 130 mM KCl, 20 mM HEPES, pH 7.4, 1 mM ATP, 1 mM MgCl₂, 1 mM PMSF. The sample was then applied on a glycerol step gradient (30–12% glycerol) and centrifuged for 15 h at 25,000 rpm (SW 32 rotor, Beckman). The separation and distribution of proteins was confirmed by SDS-PAGE gel (4–20% Mini-PROTEAN® TGX™ Precast Protein Gels, Biorad). Fractions containing high molecular weight species were pooled together and concentrated to $<500 \mu\text{L}$ using a 100-kDa cutoff concentrator. The sample was loaded on a Superose 6 10/300 Increase column (Cytiva) equilibrated in 0.05% (w/v) digitonin, 130 mM KCl, 20 mM HEPES, pH 7.4, 1 mM ATP, 1 mM MgCl₂, 1 mM PMSF. Fractions of a peak around 11 mL elution volume were analyzed using a mass photometer (Refeyn OneMP), pooled and concentrated to 8 mg/mL.

Vesicle preparation—Ghost membranes ($\sim 100 \text{ mg}$) were pelleted ($6,000 \times g$, 10 minutes), washed 5 times in 130 mM KCl, 10 mM HEPES, pH 7.4, and then homogenized with the same buffer. The sample was sonicated using microprobe (amplitude = 30, pulse on = 5 sec, rest time = 10 sec, total pulse on = 50 sec). Large fragments are removed by centrifugation ($6,000 \times g$, 10 minutes) and the supernatant was extruded (Avanti Polar Lipid) 10 times using a 400 nm filter. After extrusion, vesicles were collected by ultracentrifugation at 35,000 rpm for 30 minutes (S120-AT3, Sorvall). The pellet, which contains vesicles, was resuspended at a final concentration of 5 mg/mL. All steps were performed at room temperature to facilitate vesicle formation.

Mass photometry (MP, iSCAMS)—Mass photometry (MP) experiments were performed using a Refeyn OneMP (Refeyn Ltd.). Data acquisition was accomplished using AcquireMP (Refeyn Ltd. 172 v2.3). Samples were evaluated with microscope coverslips. The coverslips (cover glass thickness $1 \frac{1}{2} 24 \times 50 \text{ mm}$, Corning) were washed with ddH₂O and isopropanol. Silicone templates were placed on top of the coverslip to form reaction chambers

immediately prior to measurement. The instrument was calibrated using NativeMark Protein Standards (NativeMark™ Unstained Protein Standard, Thermo Fisher). 10 µL of fresh room temperature buffer was pipetted into a well, the focal position was identified and locked. For each acquisition 1 µL of the protein (at a final concentration after dilution of 200 nM) was added to the well and thoroughly mixed. MP signals were recorded for 60 s to allow detection of at least 2×10^3 individual binding events. Data analysis was performed using the DiscoverMP software.

Cryo-EM & Cryo-ET grid preparation and data collection—3 µL of purified ankyrin complex at 8mg/mL, with a surface-active additive (0.01% (w/v) glycyrrhizic acid) was added to a glow discharged (PELCO easiGlow) holey gold grid (Quantifoil UltrAuFoil grids (R0.6/1, Au 300-mesh gold)) and blotted for 4 to 6 seconds at 4°C and 100% humidity using the Vitrobot system (ThermoFisher), before plunging immediately into liquid ethane for vitrification. Images were collected on a Titan Krios electron microscope (FEI) equipped with a K3 direct electron detector (Gatan) operating at 0.83 Å per pixel in counting mode using Leginon automated data collection software. Data collection was performed using a dose of 58 e⁻/Å² across 50 frames (50 ms per frame) at a dose rate of 16 e⁻/pix/s, using a set defocus range of -0.5 µm to -1.5 µm. A 100 µm objective aperture was used. A total of 14464 micrographs were collected.

Vesicles for cryo-ET were prepared similarly using 1.2/1.3 µm holey gold grids (Quantifoil UltrAuFoil) and blotted for 10 s using a Vitrobot Mark IV (ThermoFisher), before plunging immediately into liquid ethane for vitrification. About 100 tilt series were collected on a Titan Krios electron microscope (FEI) equipped with a K3 direct electron detector (Gatan), energy filter (Gatan) and Cs-corrector, operating at 2.077 Å per pixel in counting mode using Leginon automated data collection software⁴⁸. Tilt series were collected bi-directionally from [0:+51] degrees then [0:-51] degrees in 3 degree increments, with a dose of 3.13 e⁻/Å² across 8 frames (57 ms per frame) total dose of 112 e⁻/Å² across 36 total images per tilt series, using a nominal defocus range of -3.5 µm to -4.5 µm.

Cryo-EM data processing—The final cryo-EM data processing workflow is summarized in Figure S3. Orientation distributions, FSC plots, and validation statistics are presented in Extended Data Fig. 1c and Table 1. Maps, masks and raw movies have been deposited at EMDB (Table 1) and EMPIAR (IDs: EMPIAR-11043). Subsequent steps were performed in cryoSPARC v3.2-v3.3 unless otherwise indicated⁴⁹.

Motion correction, CTF estimation and micrograph curation: Patch-based motion correction and dose-weighting of 14464 cryo-EM movies was carried out in cryoSPARC using the Patch Motion job type. Patch-based CTF estimation was performed on the aligned averages using Patch CTF.

Particle picking: An initial round of exploratory processing was performed using Blob Picker. Ranking the micrographs by the number of particles remaining after 2D classification, 58 exemplary micrographs were selected for manual picking in order to create a training dataset for the Topaz neural network-based picker¹⁶. 1510 particles corresponding to large complexes were manually picked from 58 micrographs. Topaz was

run in training mode using a downsampling factor of 6, and an estimated number of particles per micrograph of 200. The resulting model was used to pick particles using Topaz Extract. 1.8M particles were initially extracted in a box of 600 pixels, and Fourier cropped to 150 pixels for initial cleanup (2D and initial 3D classification).

2D classification: Multiple rounds of 2D classification were performed in order to isolate homogeneous subsets of particles to use for ab initio reconstruction of compositionally distinct classes. The 48 most occupied 2D classes from the initial round of 2D classification are presented in Extended Data Fig. 1b.

Initial model generation: Heterogeneous ab initio reconstruction was performed on a variety of subsets of particles selected by 2D classification, in order to generate a diverse range of initial models representing distinct 3D classes in the data for further classification.

Initial 3D classification: Heterogeneous refinement was performed using the Topaz picked initial particle stack of 1.8M particles, with 12 representative initial reconstructions as map inputs. 4 well defined, high-resolution classes of the ankyrin complex were identified, as well as several well-defined classes of smaller particles, most of which were identified as free band 3 dimers. 710k particles corresponding to ankyrin complexes were re-extracted with recentering in a 450 px box.

Consensus refinement: An initial refinement of all 710k ankyrin complex particles was performed using non-uniform refinement with on-the-fly refinement of per particle defocus, and global refinement of beam tilt and trefoil aberrations, giving an initial consensus refinement with a resolution of 2.3 Å. The use of dynamic masking and real-space windowing of particle images during refinement was disabled. Masked refinements of the Rh trimer, ankyrin-1 membrane binding domain, protein 4.2, the cytoplasmic domains of Band3-I and the transmembrane domains of Band3-I were performed starting from the global consensus refinement with local angular searches.

Sub-classification of ankyrin complex particles: Based on sub-classification of each of the original four classes, six non-redundant classes were identified. The 710k stack of clean ankyrin complex particles from the consensus refinement was subjected to heterogeneous refinement using these six classes as inputs, as well as five decoy classes, using an initial lowpass filter of 50 Å and a batch size per class of 5000 particles. The composition and occupancy of the resulting classes is summarized in Figure S5.

Sub-classification using 3D Variability Analysis: In the case of Band 3-I, Band3-II, Band3-III and AQP1, another approach was taken to isolate a set of particles with improved density for the mobile component (Extended Data Fig. 6). First, a local refinement with a mask around the mobile component was performed, yielding a relatively poor resolution, noisy local reconstruction (3.8 Å in the case of Band 3-I starting from the consensus refinement). Then, 3D variability analysis was performed as implemented in CryoSPARC 3.2, selecting five modes, with a filter resolution of 3–4.5Å. Reconstructions were calculated along each mode, and a mode corresponding to an order-disorder transition of the mobile sub-region was identified. This mode was then used (using the 3D Variability Analysis

Display job type) to split the particles into 20 clusters, and a reconstruction calculated for each. Particles belonging to clusters with well-defined, high-resolution features were combined, re-aligned globally by non-uniform refinement, and subjected to another round of local refinement. In the case of Band 3-I local refinement from the consensus refinement of all ankyrin-1 complexes, this yielded a map with a resolution of 2.8 Å.

Processing of free band 3-GPA dimer particles: In a separate processing pathway, after identification of the free band 3 dimer class using multi class ab initio reconstruction, several successive rounds of heterogeneous refinement were performed using a single band 3 dimer class and eight random density decoys, against the original 1.8M particle stack. This allowed isolation of a subset of 37k particles which were re-extracted in a 320px box and refined with non-uniform regularization to obtain a reconstruction at 2.8 Å resolution. Training a Topaz model and repicking the dataset with a model biased towards band 3-GPA dimer particles provided a substantial increase in the number of high-quality particles, and resulted in a 2.3 Å reconstruction from 166k particles.

Local refinements and generation of composite maps: For the consensus refinement, Class 1 and Class 2, local refinements using several different masks were performed to generate local reconstructions with improved density. Maps were post-processed by density modification, soft masking outside the refinement mask, and cropping to a minimal box using phenix.resolve_cryo_em (without using an atomic model in the analysis), and resampled to 0.415 Å per pixel using relion_image_handler, in order to best visualize high resolution structural details. For deposition of each local refinement, the density modified, cropped and resampled map has been designated as the main map, with non-density modified half maps that have been cropped and resampled to match the map used for model building. Raw half maps, and an optimally B-factor sharpened full reconstruction, are provided as additional maps for each deposition. In order to aid model building of the complex, composite maps of the consensus (all classes combined), Class 1 and Class 2 were generated by aligning all the relevant local maps to the matching global reconstruction, and then combining them by taking the maximum value at each voxel using UCSF Chimera⁵⁰. Composite maps were created from both the density modified maps, and the unsharpened, unmasked local maps, and both have been provided in each composite map deposition, along with the global reconstruction (and matching half maps) as additional maps.

Cryo-EM data validation: Map resolution was estimated using the gold-standard FSC=0.143 criterion, calculated from half maps using a soft mask in Relion 3.1⁵¹. Detailed validation statistics are provided in Table 1.

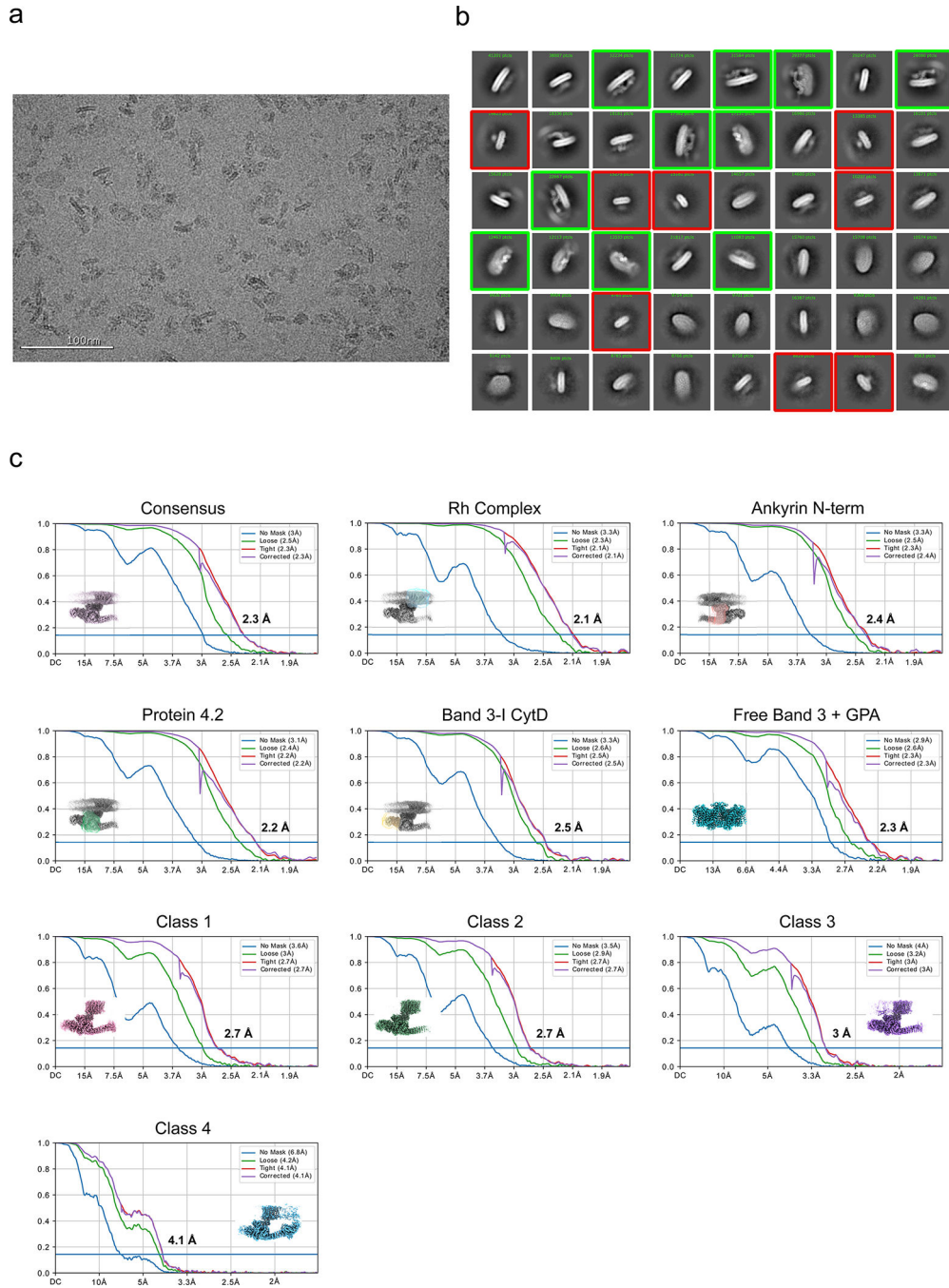
Atomic model building and refinement—An initial model for protein 4.2 was generated using trROSETTA⁵². Ankyrin-1⁵³ (PDB ID: 1N11), Band 3^{54,55} (PDB IDs: 4YZF & 1HYN) and aquaporin crystal structures⁵⁶ (PDB ID: 4CSK) were used as initial models for building the corresponding proteins. Initial models for RhCE and RhAG were generated by threading using CHAINSAW⁵⁷ as implemented in the CCP4 package⁵⁸, using the structure of the RhCG homotrimer as a template⁴² (PDB ID: 3HD6). Initial models were placed in corresponding local refinements and fit as rigid bodies

using UCSF Chimera⁵⁰. Each sub-model was then manually extended and completed in COOT^{59,60,61}, waters and ligands were added where justified by the density and chemical environment, and each final model was refined against the local map using phenix.real_space_refine⁶². Finally, models were fit to the composite map, merged, then flexibly fit using phenix.real_space_refine. The combined model of Class 1a was rigid body fit to the ankyrin-1 complex sub-tomogram average, after which ligands, waters, and sidechains were stripped, leaving a polyalanine model. Figures were prepared using UCSF ChimeraX⁶³. Refinement and validation statistics are provided in Table 1.

Cryo-ET data processing—Tilt images were frame aligned with MotionCor2⁶⁴ without patches or dose weighting. Frame aligned tilt images were used for fiducial-less tilt-series alignment in Appion-Protomo^{65,66,67}. Aligned tilt-series were dose weighted in Appion-Protomo using equation 3 in Grant & Grigorieff⁶⁸ reconstructed for initial visualization with Tomo3D^{69,70} SIRT and separately without dose weighting with Warp⁷¹. 7 binned by 4 Warp tomograms (pixel size 8.308 Å) were used to train an IsoNet⁷² model (where 300 sub-tomograms were extracted at 963 voxels after masking with z-axis cropping to remove void volumes, then trained over 35 iterations), which was then applied to each tomogram for visualization with IMOD⁷³.

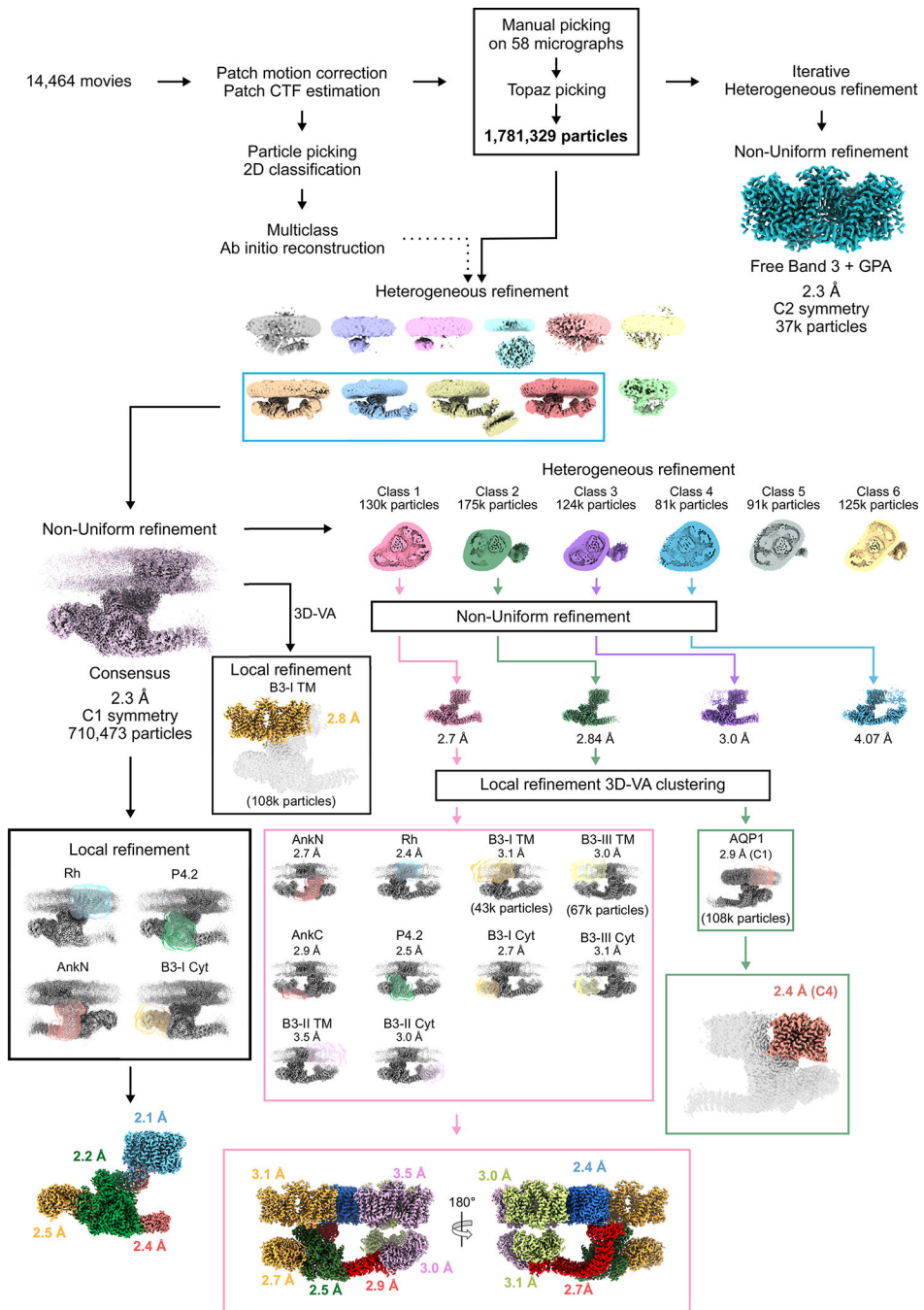
Cryo-ET subtomogram averaging—Tilt images were frame aligned with MotionCor2⁶⁴ without patches or dose weighting. The unaligned tilt images were imported into Warp⁷¹ after CTF pre-processing using Warp from the frames. The tilt-series were aligned with AreTomo⁷⁴ and the alignment files were imported back into Warp, where CTF correction was performed. Tilt-series that had poorly modeled CTFs were manually removed. Tomogram reconstruction was performed in Warp at 8.308 Å/pix. The missing wedge was corrected using IsoNet (as described above) to enhance visualization for particle picking. Twenty missing wedge corrected tomograms were manually picked with crYOLO⁷⁵ to obtain 10,000 particle coordinates. The particle coordinates were used to train crYOLO on uncorrected tomograms. Prediction was performed on 60 tomograms where a total of 60,029 particles were obtained. The particles were extracted in Warp at 4 Å/pix with a box size of 80 pixels. Initial models were generated in Relion4 using stochastic gradient descent, with 8 classes requested. The resulting initial map that most closely resembled the ankyrin-1 complex was low-pass filtered to 60 Å and used for multiple rounds of 3D classification in Relion 4^{76,77} with a spherical mask of 300 Å at an angular sampling interval of 7.5 degrees. After 3D classification, 1,596 particles were re-extracted in a 140 pixel box and used for refinement in Relion 4 with a soft spherical mask, giving a final map with a nominal resolution of 25 Å.

Extended Data



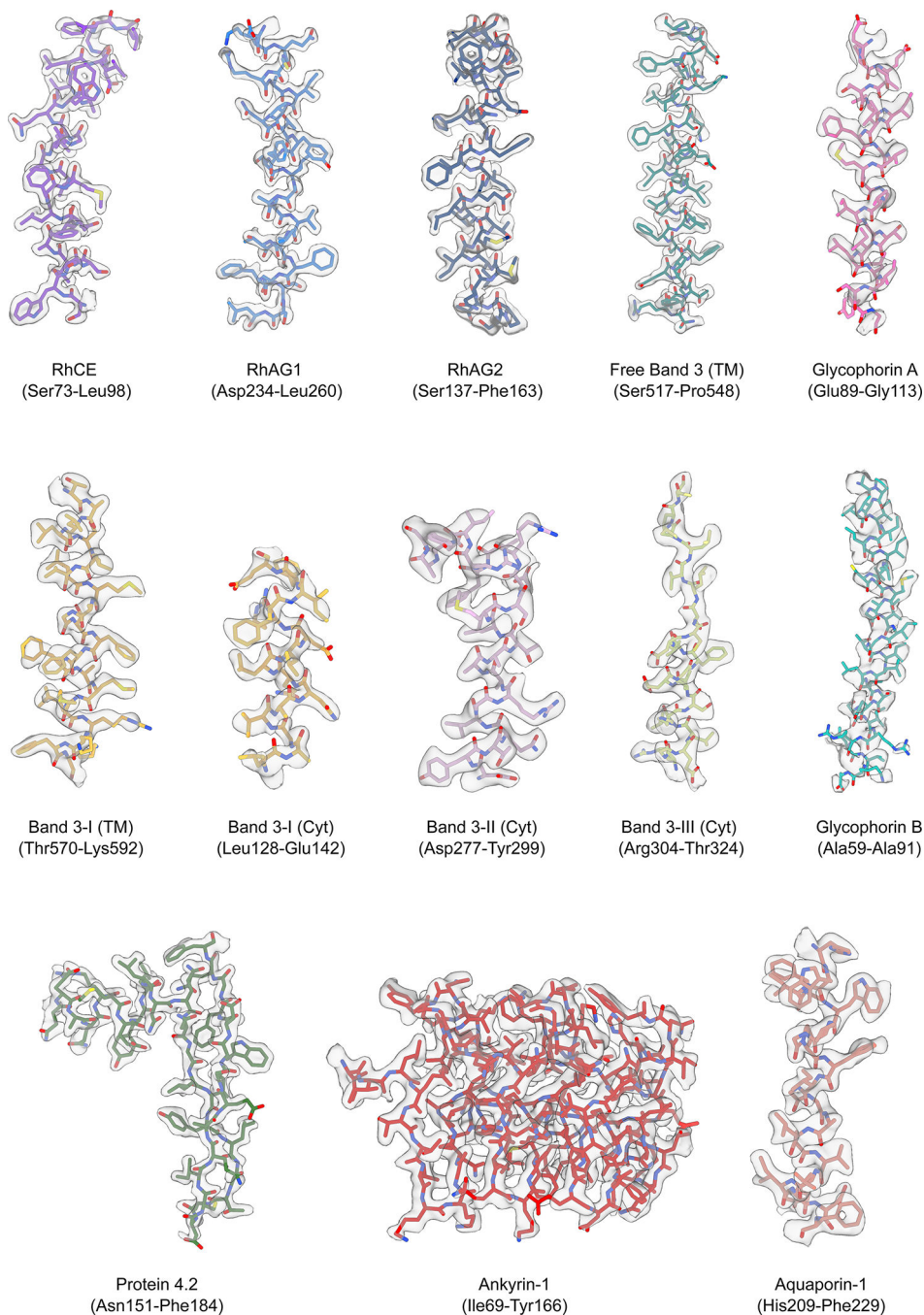
Extended Data Fig. 1. Single particle cryo-EM structure determination.

a, A representative micrograph out of 14.464 micrographs. **b**, 2D class averages of particles initially picked with Topaz (~1.8 M), ordered by population. 2D class averages of band 3-GPA (red box) and ankyrin-1 complexes (green box) are highlighted. **c**, Fourier shell correlation (FSC) curves. Maps shown as inset, with refinement mask in the case of local refinements.



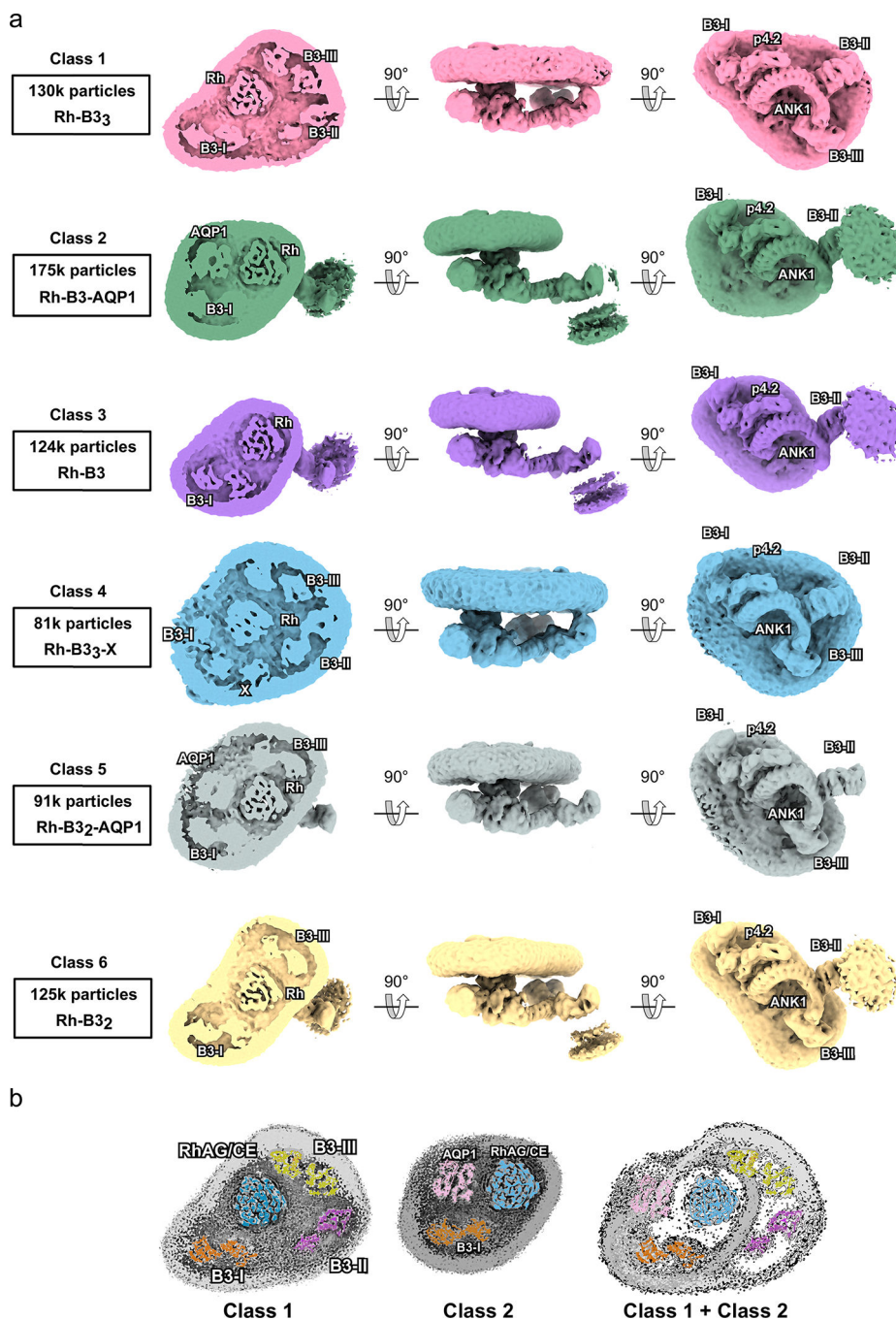
Extended Data Fig. 2. Cryo-EM workflow and analysis of the ankyrin-1 complex.

Flowchart outlining cryo-EM image acquisition and processing performed to obtain the structure of ankyrin-1 complex. All processing was performed using CryoSPARC v.3.3 (see Methods for details).



Extended Data Fig. 3. Model/map fit

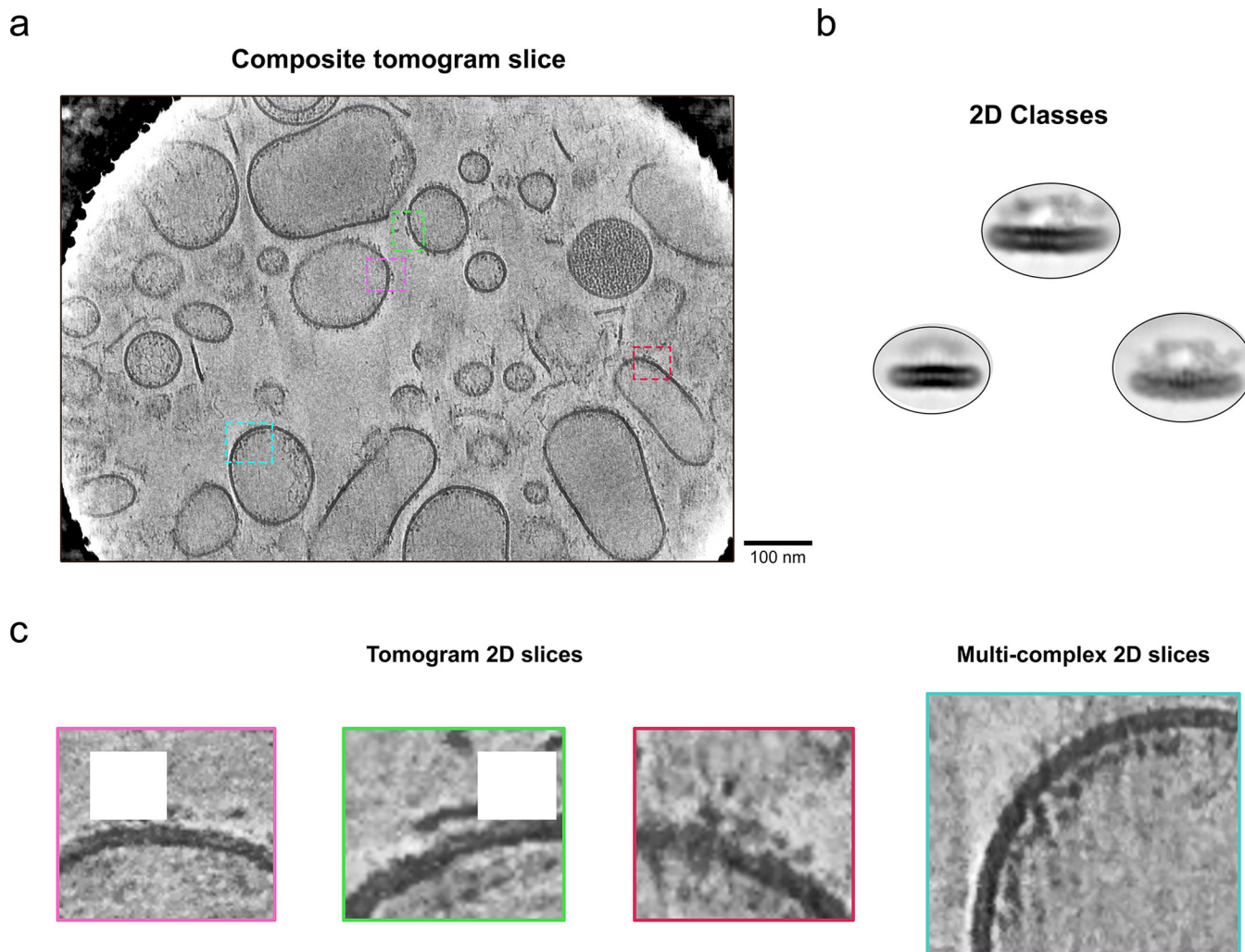
Cryo-EM densities (transparent gray surface) are shown with corresponding segments of the atomic model; sidechains are rendered in stick representation and colored as in Figure 1. The densities for GPA and free band 3 are derived from the free band3 class. Density for band 3-I TM derives from local refinement of Class 3. For all the other images we used the density from local refinement of the consensus refinement.



Extended Data Fig. 4. Ankyrin-1 complex classes.

a, Different views of six main classes of the ankyrin-1 complex. Class 1 contains an (RhAG)₂(RhCE) heterotrimer, ankyrin-1, protein 4.2, and three band 3 dimers (I, II, III). Class 2 exhibits a smaller micelle, retaining the core (RhAG)₂(RhCE)(Ank1)(P4.2) architecture, but including only one band 3 dimer (B3-I), bound to protein 4.2, and aquaporin. Class 3 contains an (RhAG)₂(RhCE) heterotrimer, and a single band 3 (B3-I). Class 4 has a bigger micelle and contains an (RhAG)₂(RhCE) heterotrimer, ankyrin-1, protein 4.2, three band 3 dimers and an unidentified protein “X”. Class 5 contains an

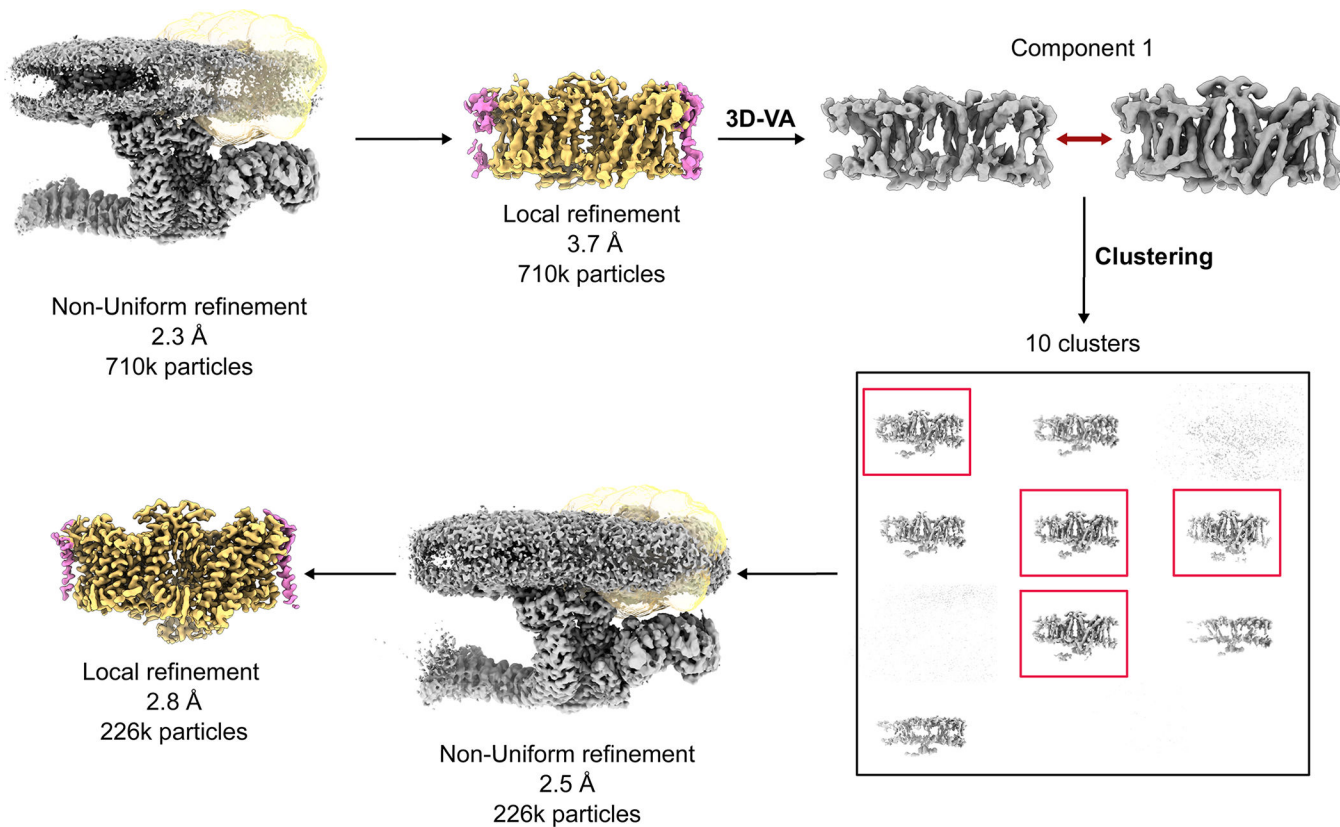
(RhAG)₂(RhCE) heterotrimer, ankyrin-1, protein 4.2, aquaporin and Band 3-I and Band 3-III. Class 6 contains an (RhAG)₂(RhCE) heterotrimer, ankyrin-1, protein 4.2, and Band 3-I and Band 3-III. In all the six classes the cytosolic domain of Band 3-II is present. The transmembrane domains of B3-II in classes 2, 3 and 6 appear to be associated with a separate micelle, likely due to either partial dissociation during extraction and/or re-association with free band 3 dimers post-extraction. **b**, Comparison of Class 1 & Class 2. Rh is colored in blue, Band 3-I in orange, Band 3-II in lilac, Band 3-III in yellow and aquaporin in pink. Superposition of Class 1 and Class 2 shows that presence of the additional two band 3 dimers does not exclude the presence of aquaporin.



Extended Data Fig. 5. Cryo-ET of native membrane vesicles.

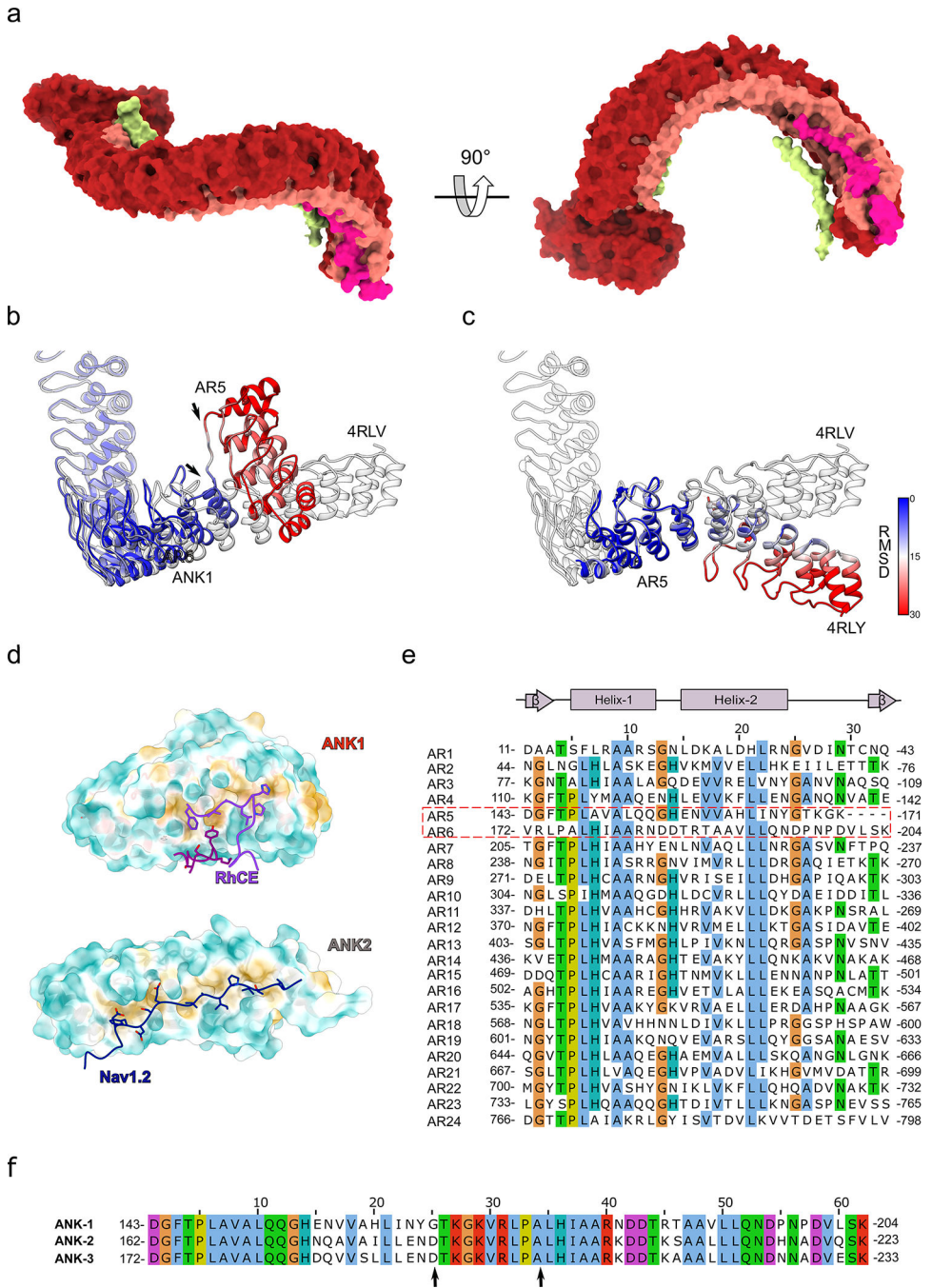
a, A composite slice from the tomogram shown in Movie S2 with several densities resembling ankyrin-1 complex side-views boxed out. **b**, SPA 2D class side-views for comparison with the tomogram slices. **c**, Magnified tomogram slices from the boxed-out regions in A. The multi-complex 2D slice on the right shows one of many visible strings of ankyrin-1 complex-like densities suggesting potential higher order assemblies. Tomogram slices are 8.3 Å thick. During the process of vesicle formation, vesicles can form in either

the native or inverted configurations, with the cytosolic side of the membrane oriented in either direction.



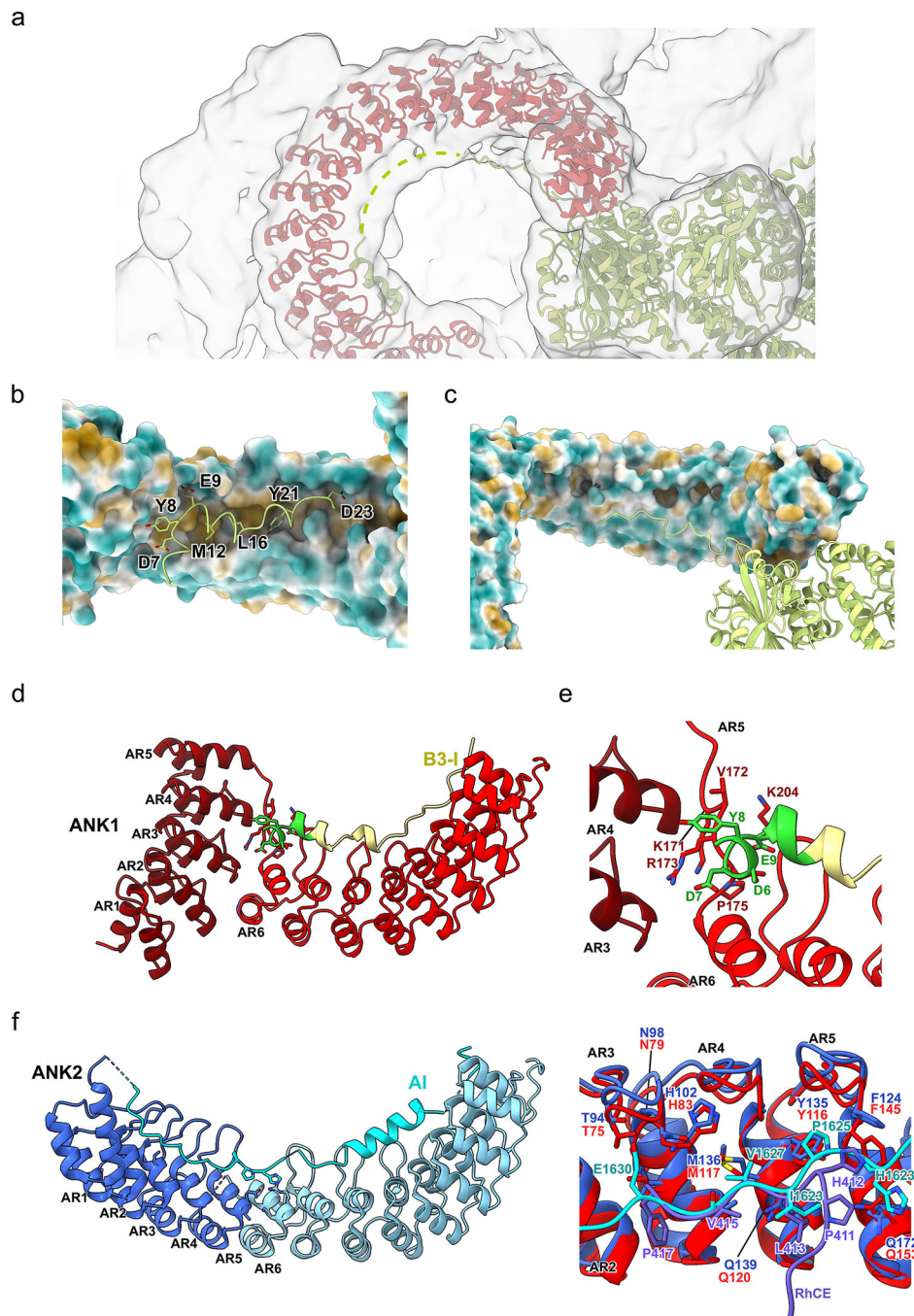
Extended Data Fig. 6. Cryo-EM workflow for sub-classification of Band 3-I from the consensus refinement.

Flowchart outlining cryo-EM processing performed to improve the structure of Band 3-I (orange) and the bound GPA proteins (magenta). All processing was performed using CryoSPARC v.3.3. A similar procedure was used to improve the density of AQP1 starting from Class 2.



Extended Data Fig. 7. Conformation of membrane-associated ankyrin-1.
a, Ankyrin structure shown as a molecular surface with the inner groove depicted in pink, the convex outer surface in red, in yellow the N-terminal peptide of Band 3-III and in magenta the C-terminal linker of ankyrin-1. **b**, Structural alignment between ankyrin-1 structure (colored by RMSD) and ankyrin-2 (in gray). The first 5 repeats of Ank1 are dramatically rearranged compared to their position in the Ank2 structure. Arrows indicate AR5 and 6. **c**, Structural alignment between ankyrin-2 (gray) and ankyrin-2 bound to Nav1.2 peptide (colored by RMSD), shows that flexibility at this interface also occurs in ankyrin-2.

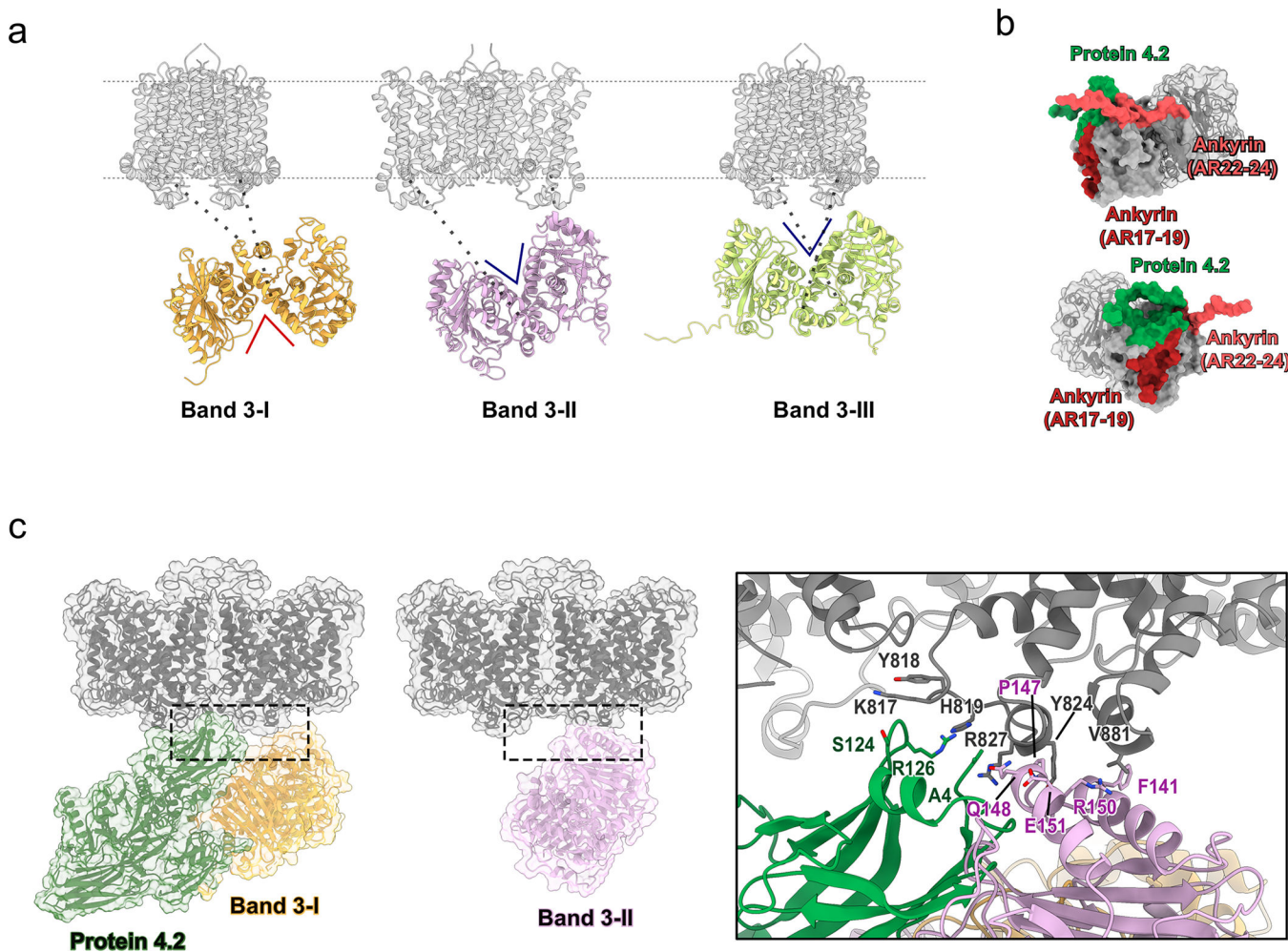
d, Hydrophobic surface calculated for the first 5 ankyrin repeats (AR1–5) of Ank1 (top) and Ank2 (bottom). RhCE N-terminal (magenta) and C-terminal fragments (purple) are displayed in stick representation. In the lower figure Ank2 is bound to Nav1.2 peptide (blue). **e**, Sequence alignment of all the 24 ankyrin repeats of Ank1 using MUSCLE⁸² and visualized and colored using Jalview with the ClustalX color scheme. The sequences for AR5 and 6 are outlined in red. **f**, Sequence of AR5 and AR6 from Ank1, Ank2 and Ank3, aligned using MUSCLE⁸² and visualized and colored using Jalview with the ClustalX colour scheme. The three sequences are well conserved in AR5 and 6. Arrows indicate the region that rearranges in Ank1. AR5 is shorter than the other repeats by 4 residues, and AR6 lacks both the “S/TP” motif at positions 4–5, and the consensus “GH” motif at positions 13–14 is replaced by two aspartates.



Extended Data Fig. 8. Ankyrin interaction with Band 3-III N-terminal peptide.

a, Map at low density threshold allows tracing of the complete Band 3-III N-terminal peptide (dotted yellow line), that runs back along the inner ankyrin groove. **b-c**, Molecular surface of the ankyrin repeats, colored by hydrophobicity, bound to the N-terminal peptide of Band 3-III (yellow). Residues 2–24 of Band 3-III form an ordered interaction with AR6–10 and the AR5–6 linker. Key residues are displayed as sticks. Band 3-III is shown as yellow ribbons. **d**, Structural comparison between ankyrin-1 (top) and ankyrin-2 structures (PDB: 4Y4D) (bottom). Structure of ankyrin-1 (dark red AR1–5 and red AR6–12) is associated

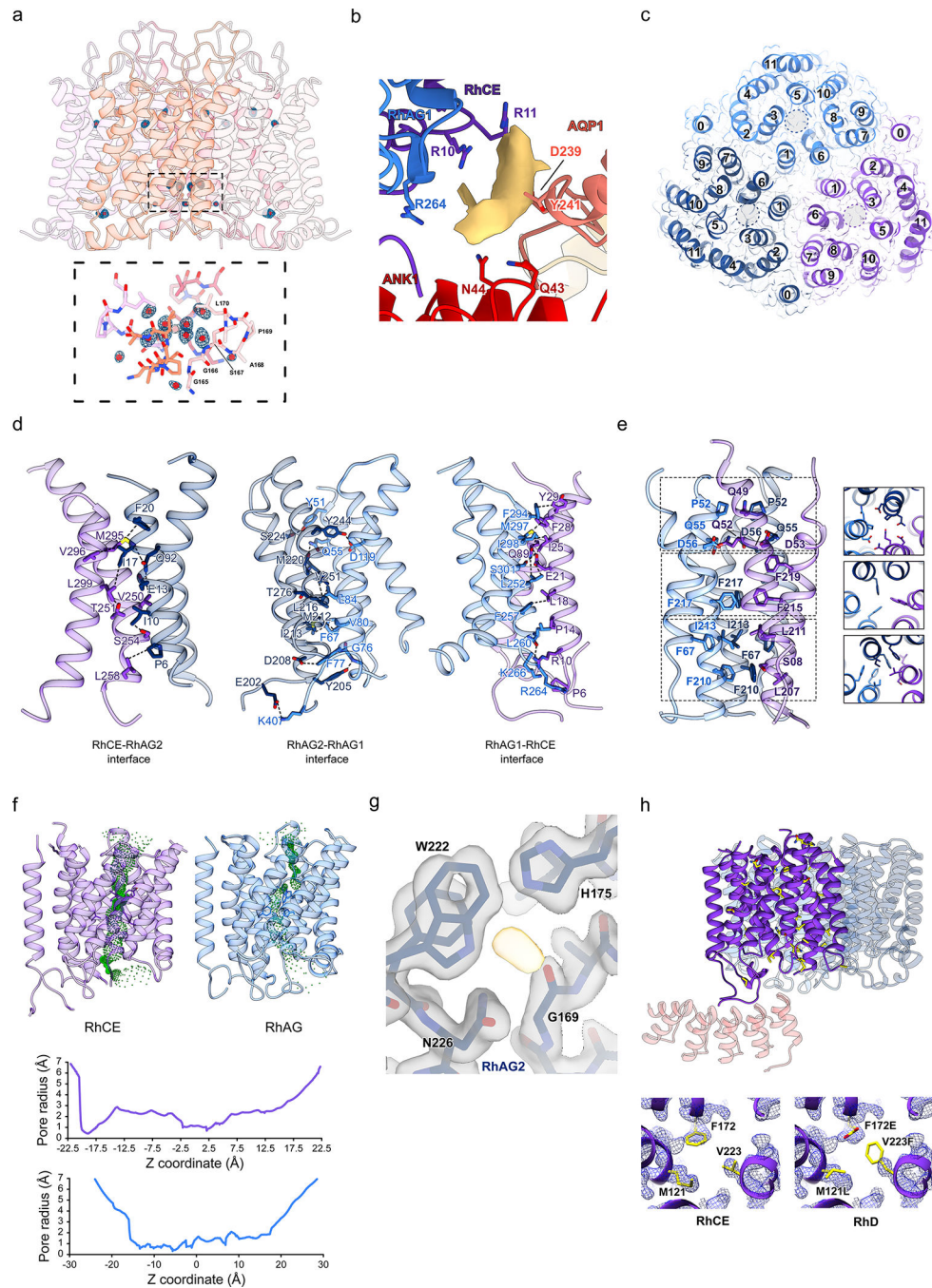
with N-terminal peptide of Band 3-I (yellow) and ankyrin-2 (dark blue AR1–6 and light blue AR6–12) is associated with the autoinhibitory domain (AI) of ankyrin-1. **e**, Close up of the AR5–6 of ankyrin-1 in panel S8d. The Band 3-I part colored in green corresponds to the first 11 N-terminal amino acids. **f**, Structural alignment between the first five ankyrin repeats (AR1–5) of ankyrin-1 (dark red) bound to RhCE peptide and ankyrin-2 (dark blue) bound to the autoinhibitory peptide of ankyrin-1. The key conserved residues that mediate the interactions between ANK1 and B3-III and ANK2 and the autoinhibitory region are shown as sticks.



Extended Data Fig. 9. Flexibility of band 3 cytosolic domain.

a, Models of the three Band 3 dimers (I, II, III). The three cytosolic domains of Band 3 proteins in the complex have different orientations. The Band 3-I cytoplasmic domain is inverted with respect to those of Band 3-II and Band 3-III. The TM part of Band 3 is colored gray. **b**, Two different views of band 3 cytosolic domain represented as molecular surface. Interacting surfaces of band 3 are distinct and non-overlapping. Regions of the band 3 cytosolic domain that interact with proteins in the complex are shown in different colors: green for the region that interact with protein 4.2, red for ankyrin repeats 22–24 and purple for ankyrin repeats 17–19. **c**, Comparison between Band 3-I (yellow) associated with

protein 4.2 (green) and Band 3-II (lilac). The model is displayed as ribbon and the surface is shown in transparency. In the right panel a close view of the interactions between Band 3-II cytosolic domain (lilac) and protein 4.2 (green); the two share the same interaction site with the TM part. Key residues for the interaction are displayed as sticks.



Extended Data Fig. 10. (RhAG)2(RhCE) trimer interactions.

a, Model of AQP1 with waters (red dots fit inside the map). In the bottom inset a close view of the waters in the central cavity. **b**, Unmodeled density at the interface of aquaporin-1

(salmon) with RhCE (purple) and RhAG (light blue). Potential interacting sidechains are depicted in stick representation. **c**, The structure of (RhAG)₂(RhCE) trimer as viewed from the cytoplasm, RhCE is colored in purple, RhAG1 in light blue and to RhAG2 in dark blue. The cryo-EM density map of the (RhAG)₂(RhCE) trimer is shown in transparency. The 12 TM helices are numbered (0–11) for each Rh molecule. Gray circles shown the pore position in each subunit. **d**, Interfaces between the three different subunits, with key residues represented as sticks. **e**, Interface between the three Rh protomers. The key residues that mediate the interactions in the interfaces are shown as sticks. Three different parts of the trimerization interface are show in the right figure viewed from the top. **f**, Analysis of the pores of RhCE and RhAG. Figure of the pore in green generated by HOLE. 2D graph of pore radius for RhCE (top graph) and RhAG (bottom graph). **h**, Close up of RhAG2, the map shows an undefine density. The key residues that interact with the undefined density are shown as sticks. **g**, Structure of (RhAG)₂(RhCE) complex and the first five repeats of ankyrin. The amino acids depicted in yellow sticks highlight the sites of variation between RhCE and RhD. Three sites of variation between RhD and RhCE are shown in the right panels, with the density map overlaid. The density map is consistent with the presence of RhCE, not RhD.

Supplementary Material

Refer to Web version on PubMed Central for supplementary material.

Acknowledgments:

CryoEM data were collected at Columbia Cryo-EM facility and at the Simons Electron Microscopy Center (SEMC), directed by Dr Bridget Carragher and Dr Clint Potter, with the assistance of staff from both SEMC and the Columbia University Cryo-Electron Microscopy Center. Bob Grassucci and Zhening Zhang from the Columbia CryoEM Center assisted with data collection. Some of the work was performed using equipment from the Center for Membrane Protein Production and Analysis (COMPPA; NIH P41 GM116799 to Wayne A. Hendrickson). The authors thank Dr. Lorenzo Maso for generating the schematic representation of the ankyrin-1 complex (Fig. 1c) and Dr. Filippo Mancina and his lab members for support and critical reading of the manuscript. We are grateful to Dr. Paola Berto and Dr. Lucia Barazzuol, Department of Biomedical Sciences, University of Padova, for their support in the preparation of the ghost membranes. We thank the “Centro Transfusionale dell’Azienda Ospedaliera Università di Padova” and the individuals who donated their blood from which the ankyrin complex was purified. T.C. is supported by grants from the Italian Ministry of University and Research (Bando SIR 2014 no. RBSI14C65Z and PRIN2017) and from the Università degli Studi di Padova (Progetto Giovani 2012 no. GRIC128SP0, Progetto di Ateneo 2016 no. CALI_SID16_01 and STARS consolidator grant 2019). Some of this work was performed at the Simons Electron Microscopy Center, National Resource for Automated Molecular Microscopy and the National Center for In-situ Tomographic Ultramicroscopy located at the New York Structural Biology Center, supported by grants from the Simons Foundation (SF349247) and NIH NIGMS (GM103310), and NIH (U24GM139171).

Data availability:

All raw movie files, aligned micrographs, and particle coordinates (in two STAR files, one for band 3-GPA and one for the ankyrin complexes) are deposited in the EMPIAR (EMPIAR-11043). The cryo-EM density maps and models have been deposited in the Electron Microscopy Data Bank and the Protein Data Bank. PDB IDs: 7UZ3, 7UZE, 7UZQ, 7UZS, 7UZU, 7UZV, 7V07, 7V0K, 7V0M, 7V0Q, 7V0S, 7V0T, 7V0U, 7V0X, 7V0Y, 7V19, 8CRQ, 8CRR, 8CRT, 8CS9, 8CSV, 8CSW, 8CSX, 8CSY, 8CT2, 8CT3, 8CSL, 8CTE.

EMDB IDs: EMD-26874, EMD- 26886, EMD-26916, EMD-26917, EMD-26918, EMD-26919, EMD-26940, EMD-26943, EMD-26944, EMD-26948, EMD-26949, EMD-26950, EMD-26951, EMD-26952, EMD-26953, EMD-26954, EMD-26955, EMD-26956, EMD-26958, EMD-26960, EMD-26972, EMD-26973, EMD-26974, EMD-26975, EMD-26978, EMD-26979, EMD-26982, EMD-26965, EMD-26988.

References:

1. Marchesi VT & Steers E Selective Solubilization of a Protein Component of the Red Cell Membrane. *Science* 159, 203–204 (1968). [PubMed: 5634911]
2. Unsain N, Stefani FD & Cáceres A The Actin/Spectrin Membrane-Associated Periodic Skeleton in Neurons. *Front Synaptic Neurosci* 10, 10 (2018). [PubMed: 29875650]
3. Bennett V & Stenbuck PJ Identification and partial purification of ankyrin, the high affinity membrane attachment site for human erythrocyte spectrin. *J Biol Chem* 254, 2533–2541 (1979). [PubMed: 372182]
4. Bennett V & Stenbuck PJ The membrane attachment protein for spectrin is associated with band 3 in human erythrocyte membranes. *Nature* 280, 468–473 (1979). [PubMed: 379653]
5. Stevens SR et al. Ankyrin-R regulates fast-spiking interneuron excitability through perineuronal nets and Kv3.1b K⁺ channels. *Elife* 10, e66491 (2021). [PubMed: 34180393]
6. Mohler PJ, Davis JQ & Bennett V Ankyrin-B coordinates the Na/K ATPase, Na/Ca exchanger, and InsP3 receptor in a cardiac T-tubule/SR microdomain. *PLoS Biol* 3, e423 (2005). [PubMed: 16292983]
7. Jenkins PM et al. Giant ankyrin-G: a critical innovation in vertebrate evolution of fast and integrated neuronal signaling. *Proc Natl Acad Sci U S A* 112, 957–964 (2015). [PubMed: 25552556]
8. Jenkins SM & Bennett V Ankyrin-G coordinates assembly of the spectrin-based membrane skeleton, voltage-gated sodium channels, and L1 CAMs at Purkinje neuron initial segments. *J Cell Biol* 155, 739–746 (2001). [PubMed: 11724816]
9. Bennett V Purification of an active proteolytic fragment of the membrane attachment site for human erythrocyte spectrin. *J Biol Chem* 253, 2292–2299 (1978). [PubMed: 632270]
10. Perrotta S, Gallagher PG & Mohandas N Hereditary spherocytosis. *Lancet* 372, 1411–1426 (2008). [PubMed: 18940465]
11. Bennett V & Healy J Organizing the fluid membrane bilayer: diseases linked to spectrin and ankyrin. *Trends Mol Med* 14, 28–36 (2008). [PubMed: 18083066]
12. Nicolas V et al. Rh-RhAG/ankyrin-R, a new interaction site between the membrane bilayer and the red cell skeleton, is impaired by Rh(null)-associated mutation. *J Biol Chem* 278, 25526–25533 (2003). [PubMed: 12719424]
13. Jiang W et al. Interaction of glucose transporter 1 with anion exchanger 1 in vitro. *Biochemical and Biophysical Research Communications* 339, 1255–1261 (2006). [PubMed: 16343432]
14. Mankelov TJ, Satchwell TJ & Burton NM Refined views of multi-protein complexes in the erythrocyte membrane. *Blood Cells Mol Dis* 49, 1–10 (2012). [PubMed: 22465511]
15. Young G et al. Quantitative mass imaging of single biological macromolecules. *Science* 360, 423–427 (2018). [PubMed: 29700264]
16. Bepler T et al. Positive-unlabeled convolutional neural networks for particle picking in cryo-electron micrographs. *Nat Methods* 16, 1153–1160 (2019). [PubMed: 31591578]
17. Chen K, Li J, Wang C, Wei Z & Zhang M Autoinhibition of ankyrin-B/G membrane target bindings by intrinsically disordered segments from the tail regions. *Elife* 6, e29150 (2017). [PubMed: 28841137]
18. Wang C et al. Structural basis of diverse membrane target recognitions by ankyrins. *Elife* 3, (2014).
19. Toye AM et al. Protein-4.2 association with band 3 (AE1, SLCA4) in *Xenopus* oocytes: effects of three natural protein-4.2 mutations associated with hemolytic anemia. *Blood* 105, 4088–4095 (2005). [PubMed: 15692067]

20. Satchwell TJ, Shoemark DK, Sessions RB & Toye AM Protein 4.2: a complex linker. *Blood Cells Mol Dis* 42, 201–210 (2009). [PubMed: 19269200]
21. Risinger MA, Dotimas EM & Cohen CM Human erythrocyte protein 4.2, a high copy number membrane protein, is N-myristylated. *J Biol Chem* 267, 5680–5685 (1992). [PubMed: 1544941]
22. Beckmann R, Smythe JS, Anstee DJ & Tanner MJ Coexpression of band 3 mutants and Rh polypeptides: differential effects of band 3 on the expression of the Rh complex containing D polypeptide and the Rh complex containing CcEe polypeptide. *Blood* 97, 2496–2505 (2001). [PubMed: 11290615]
23. Hanicak A et al. Erythrocyte band 3 protein strongly interacts with phosphoinositides. *FEBS Letters* 348, 169–172 (1994). [PubMed: 8034035]
24. Bruce LJ et al. A band 3-based macrocomplex of integral and peripheral proteins in the RBC membrane. *Blood* 101, 4180–4188 (2003). [PubMed: 12531814]
25. Perrotta S et al. The N-terminal 11 amino acids of human erythrocyte band 3 are critical for aldolase binding and protein phosphorylation: implications for band 3 function. *Blood* 106, 4359–4366 (2005). [PubMed: 16118313]
26. Ferru E et al. Regulation of membrane-cytoskeletal interactions by tyrosine phosphorylation of erythrocyte band 3. *Blood* 117, 5998–6006 (2011). [PubMed: 21474668]
27. Ding Y, Casey JR & Kopito RR The major kidney AE1 isoform does not bind ankyrin (Ank1) in vitro. An essential role for the 79 NH₂-terminal amino acid residues of band 3. *J Biol Chem* 269, 32201–32208 (1994). [PubMed: 7798219]
28. Kim S et al. Determination of structural models of the complex between the cytoplasmic domain of erythrocyte band 3 and ankyrin-R repeats 13–24. *J Biol Chem* 286, 20746–20757 (2011). [PubMed: 21493712]
29. Chang SH & Low PS Identification of a Critical Ankyrin-binding Loop on the Cytoplasmic Domain of Erythrocyte Membrane Band 3 by Crystal Structure Analysis and Site-directed Mutagenesis. *Journal of Biological Chemistry* 278, 6879–6884 (2003). [PubMed: 12482869]
30. Bruce LJ et al. Changes in the blood group Wright antigens are associated with a mutation at amino acid 658 in human erythrocyte band 3: a site of interaction between band 3 and glycophorin A under certain conditions. *Blood* 85, 541–547 (1995). [PubMed: 7812009]
31. Williamson RC & Toye AM Glycophorin A: Band 3 aid. *Blood Cells, Molecules, and Diseases* 41, 35–43 (2008).
32. Young MT, Beckmann R, Toye AM & Tanner MJ Red-cell glycophorin A-band 3 interactions associated with the movement of band 3 to the cell surface. *Biochem J* 350 Pt 1, 53–60 (2000). [PubMed: 10926825]
33. Trenker R, Call ME & Call MJ Crystal Structure of the Glycophorin A Transmembrane Dimer in Lipidic Cubic Phase. *J Am Chem Soc* 137, 15676–15679 (2015). [PubMed: 26642914]
34. Kalli AC & Reithmeier RAF Interaction of the human erythrocyte Band 3 anion exchanger 1 (AE1, SLC4A1) with lipids and glycophorin A: Molecular organization of the Wright (Wr) blood group antigen. *PLoS Comput Biol* 14, e1006284 (2018). [PubMed: 30011272]
35. Taylor AM, Boulter J, Harding SE, Cölfen H & Watts A Hydrodynamic properties of human erythrocyte band 3 solubilized in reduced Triton X-100. *Biophys J* 76, 2043–2055 (1999). [PubMed: 10096900]
36. Su Y et al. Associations of protein 4.2 with band 3 and ankyrin. *Mol Cell Biochem* 289, 159–166 (2006). [PubMed: 16718373]
37. Hsu K et al. Adaptable interaction between aquaporin-1 and band 3 reveals a potential role of water channel in blood CO₂ transport. *FASEB J* 31, 4256–4264 (2017). [PubMed: 28596233]
38. Reithmeier RA A membrane metabolon linking carbonic anhydrase with chloride/bicarbonate anion exchangers. *Blood Cells Mol Dis* 27, 85–89 (2001). [PubMed: 11358366]
39. Vince JW & Reithmeier RA Carbonic anhydrase II binds to the carboxyl terminus of human band 3, the erythrocyte C1-/HCO₃⁻ exchanger. *J Biol Chem* 273, 28430–28437 (1998). [PubMed: 9774471]
40. Endeward V et al. Evidence that aquaporin 1 is a major pathway for CO₂ transport across the human erythrocyte membrane. *FASEB J* 20, 1974–1981 (2006). [PubMed: 17012249]

41. Planelles G Ammonium homeostasis and human Rhesus glycoproteins. *Nephron Physiol* 105, p11–17 (2007). [PubMed: 17106214]
42. Gruswitz F et al. Function of human Rh based on structure of RhCG at 2.1 Å. *Proc Natl Acad Sci U S A* 107, 9638–9643 (2010). [PubMed: 20457942]
43. Geyer RR, Parker MD, Toye AM, Boron WF & Musa-Aziz R Relative CO₂/NH₃ permeabilities of human RhAG, RhBG and RhCG. *J Membr Biol* 246, 915–926 (2013). [PubMed: 24077989]
44. Endeward V, Cartron J, Ripoche P & Gros, and G. RhAG protein of the Rhesus complex is a CO₂ channel in the human red cell membrane. *FASEB j.* 22, 64–73 (2008). [PubMed: 17712059]
45. Burton NM & Anstee DJ Structure, function and significance of Rh proteins in red cells. *Curr Opin Hematol* 15, 625–630 (2008). [PubMed: 18832935]
46. Conroy MJ, Bullough PA, Merrick M & Avent ND Modelling the human rhesus proteins: implications for structure and function. *Br J Haematol* 131, 543–551 (2005). [PubMed: 16281947]

Methods References:

47. Niggli V & Carafoli E The Plasma Membrane Ca(2+) ATPase: Purification by Calmodulin Affinity Chromatography, and Reconstitution of the Purified Protein. *Methods Mol Biol* 1377, 57–70 (2016). [PubMed: 26695022]
48. Suloway C et al. Fully automated, sequential tilt-series acquisition with Legikon. *Journal of Structural Biology* 167, 11–18 (2009). [PubMed: 19361558]
49. Punjani A, Rubinstein JL, Fleet DJ & Brubaker MA cryoSPARC: algorithms for rapid unsupervised cryo-EM structure determination. *Nat Methods* 14, 290–296 (2017). [PubMed: 28165473]
50. Pettersen EF et al. UCSF Chimera--a visualization system for exploratory research and analysis. *J Comput Chem* 25, 1605–1612 (2004). [PubMed: 15264254]
51. Zivanov J et al. New tools for automated high-resolution cryo-EM structure determination in RELION-3. *Elife* 7, e42166 (2018). [PubMed: 30412051]
52. Yang J et al. Improved protein structure prediction using predicted interresidue orientations. *Proc Natl Acad Sci USA* 117, 1496–1503 (2020). [PubMed: 31896580]
53. Michaely P, Tomchick DR, Machius M & Anderson RGW Crystal structure of a 12 ANK repeat stack from human ankyrinR. *EMBO J* 21, 6387–6396 (2002). [PubMed: 12456646]
54. Arakawa T et al. Crystal structure of the anion exchanger domain of human erythrocyte band 3. *Science* 350, 680–684 (2015). [PubMed: 26542571]
55. Zhang D, Kiyatkin A, Bolin JT & Low PS Crystallographic structure and functional interpretation of the cytoplasmic domain of erythrocyte membrane band 3. *Blood* 96, 2925–2933 (2000). [PubMed: 11049968]
56. Ruiz Carrillo D et al. Crystallization and preliminary crystallographic analysis of human aquaporin 1 at a resolution of 3.28 Å. *Acta Crystallogr F Struct Biol Commun* 70, 1657–1663 (2014). [PubMed: 25484221]
57. Stein N *CHAINS*: a program for mutating pdb files used as templates in molecular replacement. *J Appl Crystallogr* 41, 641–643 (2008).
58. Winn MD et al. Overview of the *CCP4* suite and current developments. *Acta Crystallogr D Biol Crystallogr* 67, 235–242 (2011). [PubMed: 21460441]
59. Emsley P, Lohkamp B, Scott WG & Cowtan K Features and development of Coot. *Acta Crystallogr D Biol Crystallogr* 66, 486–501 (2010). [PubMed: 20383002]
60. Emsley P & Cowtan K Coot: model-building tools for molecular graphics. *Acta Crystallogr D Biol Crystallogr* 60, 2126–2132 (2004). [PubMed: 15572765]
61. Casañal A, Lohkamp B & Emsley P Current developments in Coot for macromolecular model building of Electron Cryo-microscopy and Crystallographic Data. *Protein Sci* 29, 1069–1078 (2020). [PubMed: 31730249]
62. Afonine PV et al. Real-space refinement in *PHENIX* for cryo-EM and crystallography. *Acta Crystallogr D Struct Biol* 74, 531–544 (2018). [PubMed: 29872004]

63. Pettersen EF et al. UCSF ChimeraX: Structure visualization for researchers, educators, and developers. *Protein Sci* 30, 70–82 (2021). [PubMed: 32881101]
64. Zheng SQ et al. MotionCor2: anisotropic correction of beam-induced motion for improved cryo-electron microscopy. *Nat Methods* 14, 331–332 (2017). [PubMed: 28250466]
65. Noble AJ & Stagg SM Automated batch fiducial-less tilt-series alignment in Appion using Protomo. *Journal of Structural Biology* 192, 270–278 (2015). [PubMed: 26455557]
66. Winkler H & Taylor KA Accurate marker-free alignment with simultaneous geometry determination and reconstruction of tilt series in electron tomography. *Ultramicroscopy* 106, 240–254 (2006). [PubMed: 16137829]
67. Lander GC et al. Appion: An integrated, database-driven pipeline to facilitate EM image processing. *Journal of Structural Biology* 166, 95–102 (2009). [PubMed: 19263523]
68. Grant T & Grigorieff N Measuring the optimal exposure for single particle cryo-EM using a 2.6 Å reconstruction of rotavirus VP6. *eLife* 4, e06980 (2015). [PubMed: 26023829]
69. Agulleiro JI & Fernandez JJ Fast tomographic reconstruction on multicore computers. *Bioinformatics* 27, 582–583 (2011). [PubMed: 21172911]
70. Agulleiro J-I & Fernandez J-J Tomo3D 2.0 – Exploitation of Advanced Vector eXtensions (AVX) for 3D reconstruction. *Journal of Structural Biology* 189, 147–152 (2015). [PubMed: 25528570]
71. Tegunov D & Cramer P Real-time cryo-electron microscopy data preprocessing with Warp. *Nat Methods* 16, 1146–1152 (2019). [PubMed: 31591575]
72. Liu Y-T et al. Isotropic Reconstruction of Electron Tomograms with Deep Learning. 10.1101/2021.07.17.452128 (2021) doi:10.1101/2021.07.17.452128.
73. Kremer JR, Mastronarde DN & McIntosh JR Computer Visualization of Three-Dimensional Image Data Using IMOD. *Journal of Structural Biology* 116, 71–76 (1996). [PubMed: 8742726]
74. Zheng S et al. AreTomo: An integrated software package for automated marker-free, motion-corrected cryo-electron tomographic alignment and reconstruction. 10.1101/2022.02.15.480593 (2022) doi:10.1101/2022.02.15.480593.
75. Wagner T et al. SPHIRE-crYOLO is a fast and accurate fully automated particle picker for cryo-EM. *Commun Biol* 2, 218 (2019). [PubMed: 31240256]
76. Zivanov J et al. A Bayesian approach to single-particle electron cryo-tomography in RELION-4.0. 10.1101/2022.02.28.482229 (2022) doi:10.1101/2022.02.28.482229.
77. Kimanius D, Dong L, Sharov G, Nakane T & Scheres SHW New tools for automated cryo-EM single-particle analysis in RELION-4.0. *Biochemical Journal* 478, 4169–4185 (2021). [PubMed: 34783343]

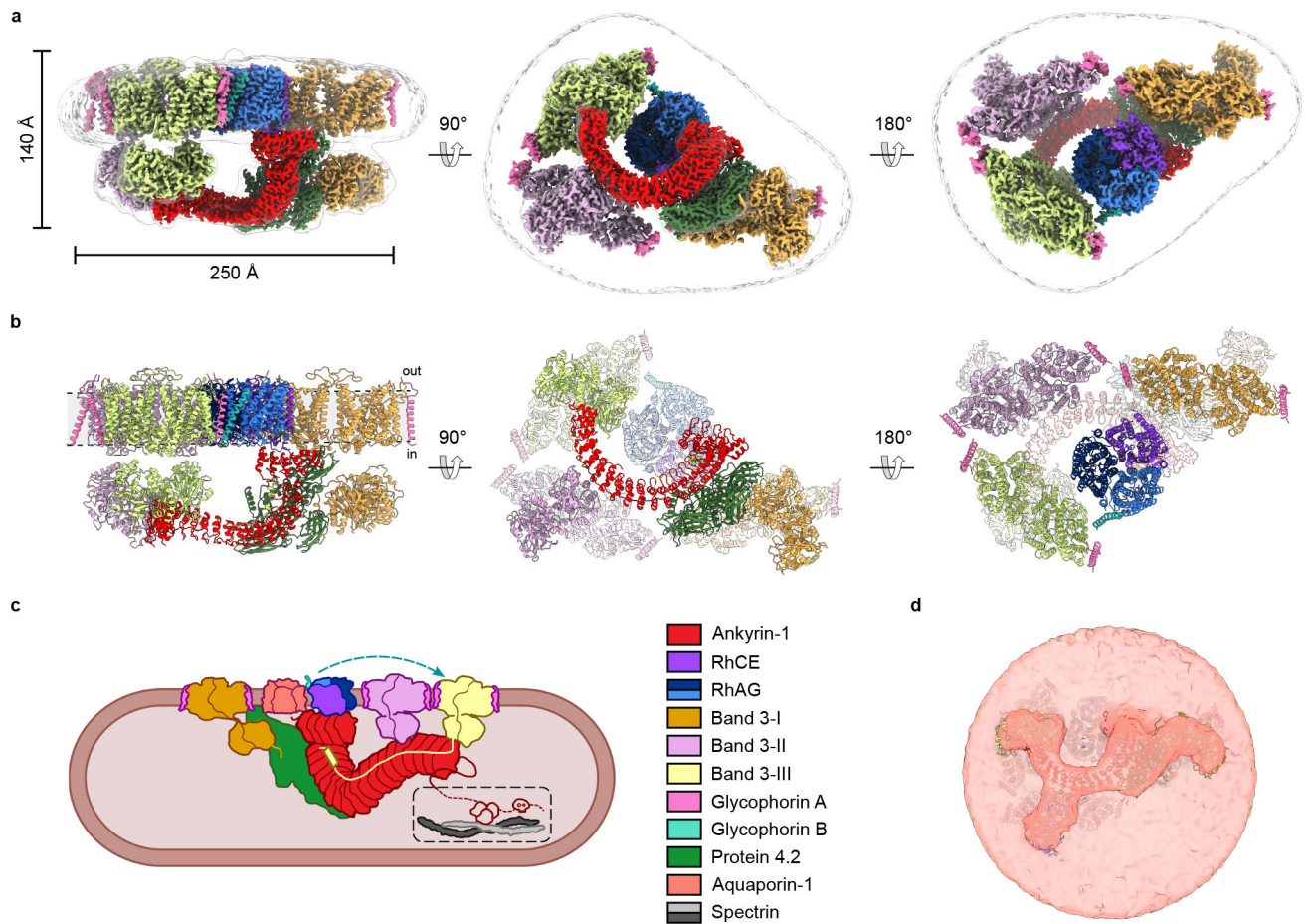


Fig. 1: Architecture of the human erythrocyte ankyrin-1 complex.

a, The overall cryo-EM density map of the ankyrin-1 complex (Class 1a; transparent white surface) shown in three different views, with local reconstructions of different regions superposed. Band 3-I, II, III are colored orange, lilac and yellow respectively; ankyrin is colored red, protein 4.2 green, RhCE purple and RhAG blue and light blue, GPA is colored in magenta and GPB in aquamarine. **b**, Model of the ankyrin-1 complex in the plane of the membrane (left panel), viewed from the cytoplasm (central panel) and from the outside of the plasma membrane (right panel). Reference colors are the same used in panel A. **c**, Schematic of the proposed ankyrin-1 complex in the RBC. Inside the dashed line the connection between ankyrin and spectrin is depicted. **d**, Sub-tomogram average of the ankyrin-1 complex from native vesicles with rigid-body fit atomic model.

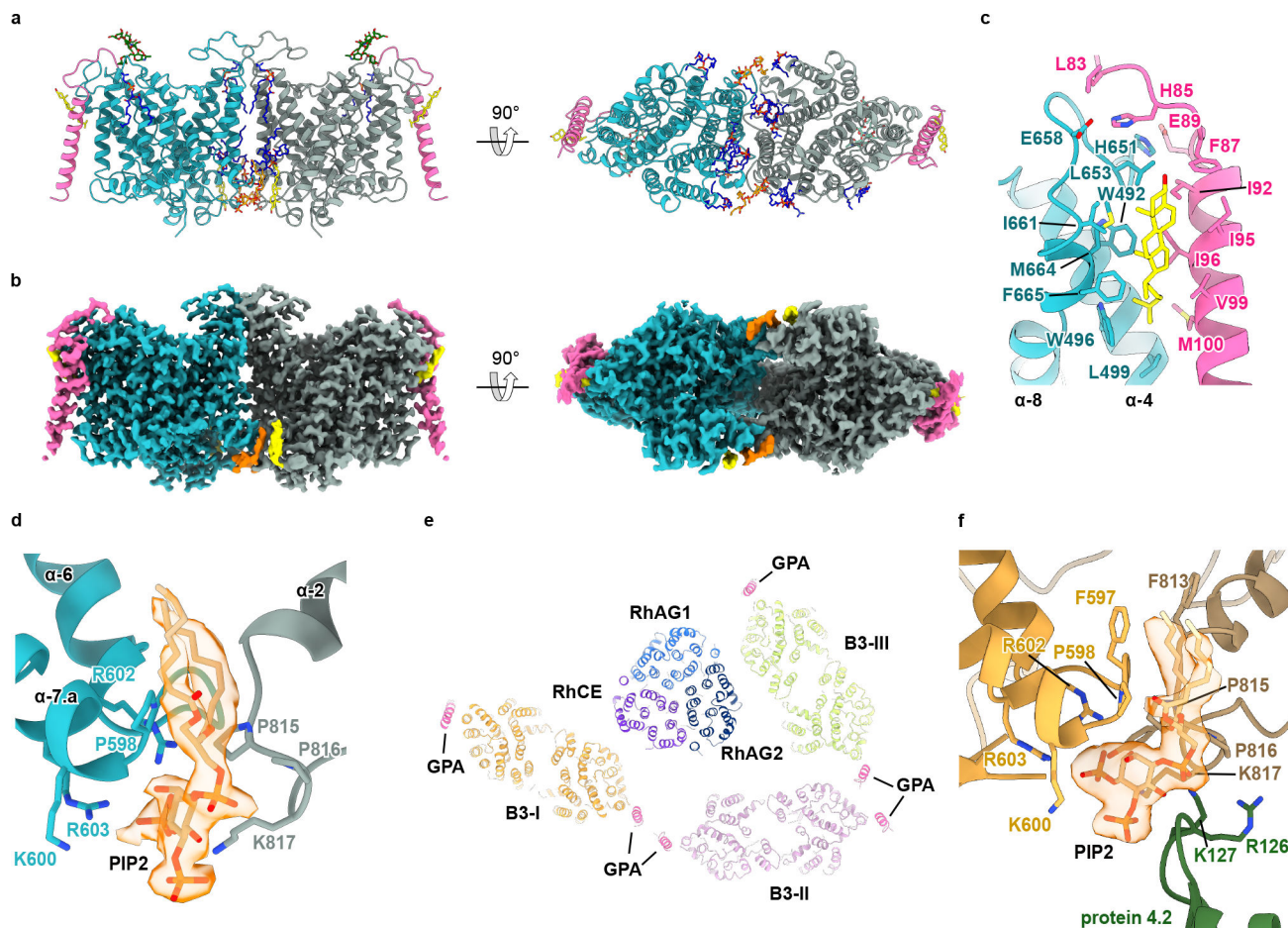


Fig. 2: Interactions between ankyrin-1 and the proteins in the ankyrin-1 complex.

a, Overview of ankyrin-1 interactions with binding partners in the ankyrin-1 complex. The proteins are depicted in cartoon representation. Transmembrane domains of band 3, GPA and GPB are omitted for clarity. Ankyrin (red) interacts with RhCE (purple) and AQP1 (salmon), and both interact with the peptide binding groove of AR1–5; protein 4.2 (green) interacts with the exterior surface of AR1 and AR6–13; Band 3-II (lilac) and Band 3-III (yellow) interact predominantly with the exterior surface of AR17–24, N-terminus domain of Band 3-III interacts also with the peptide binding groove of AR6–10. Insets refer to regions highlighted in panels B to F. On the top left of the panel a small thumbnail is included to show how the figure is positioned compare to Fig 1a **b-f**, Close-up views of the interactions between protein 4.2 and Band 3-I (orange) (**b**); ankyrin and protein 4.2 (**c**); ankyrin and RhCE (**d**); ankyrin and Band 3-II (**e**) and ankyrin and Band 3-III (**f**). The key residues that mediate the interactions in the interfaces are shown as sticks. Key interactions are indicated with black dotted lines.

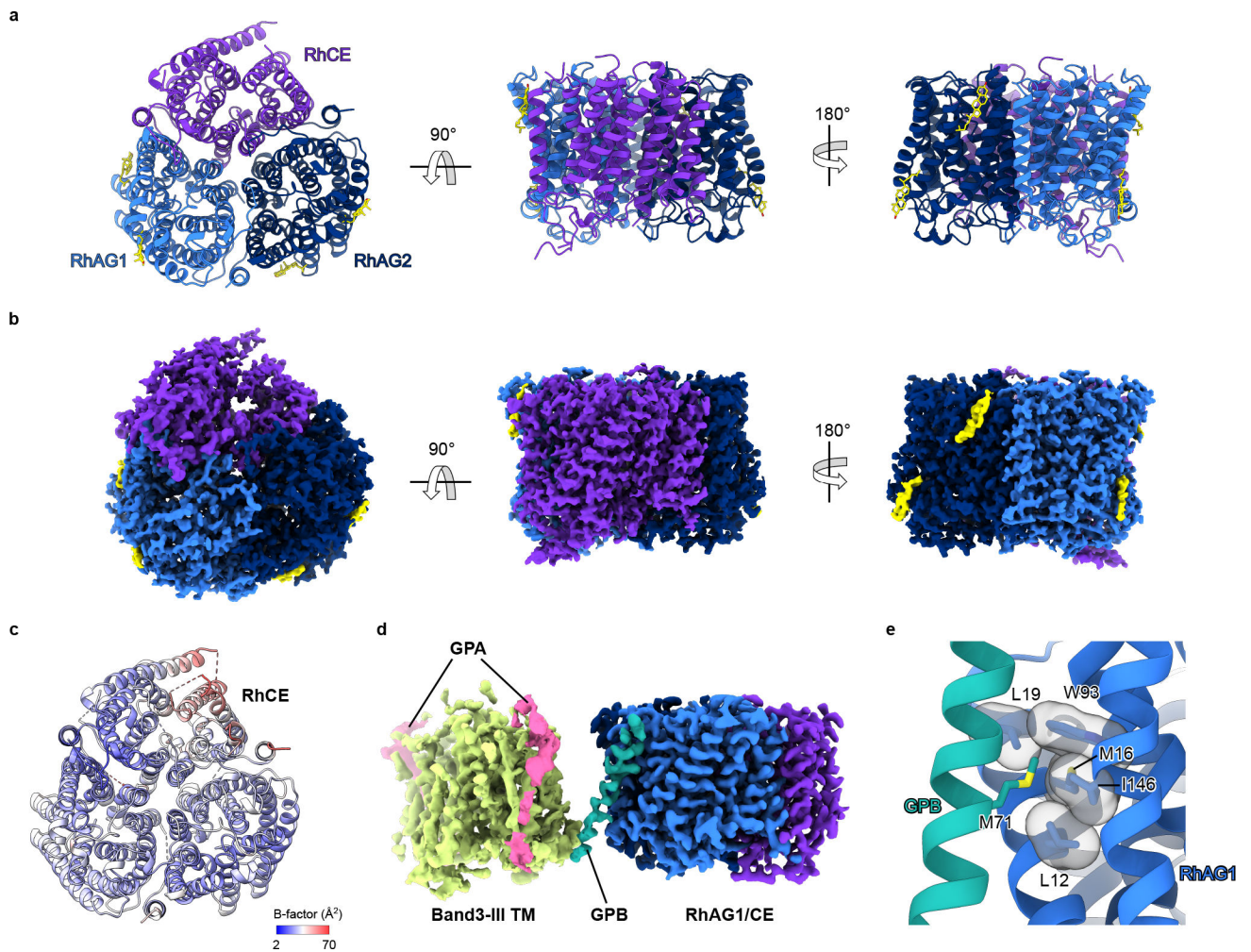


Fig. 3: Protein 4.2 is an adaptor that mediates binding of Band 3-I.

a, The 2.4 \AA cryo-EM density map of protein 4.2 from local refinement of the consensus reconstruction. **b**, Structure of protein 4.2 colored by domain from the N- (blue) to the C- (red) terminus. The four domains are labeled. The proteins are depicted in cartoon representation. **c**, Model of protein 4.2 (green) and band 3-I (orange), PIP_2 is colored in yellow. The proteins are shown in cartoon representation, and the membrane is represented in gray. **d**, The outer face of protein 4.2 forms the primary binding site for Band 3-I. Protein 4.2 is displayed as a molecular surface colored by domain from the N- (blue) to the C- (red) terminus, band 3-I cytosolic domain is displayed as ribbon, and the parts of Band 3-I that are not interacting with protein 4.2 are shown in transparency.

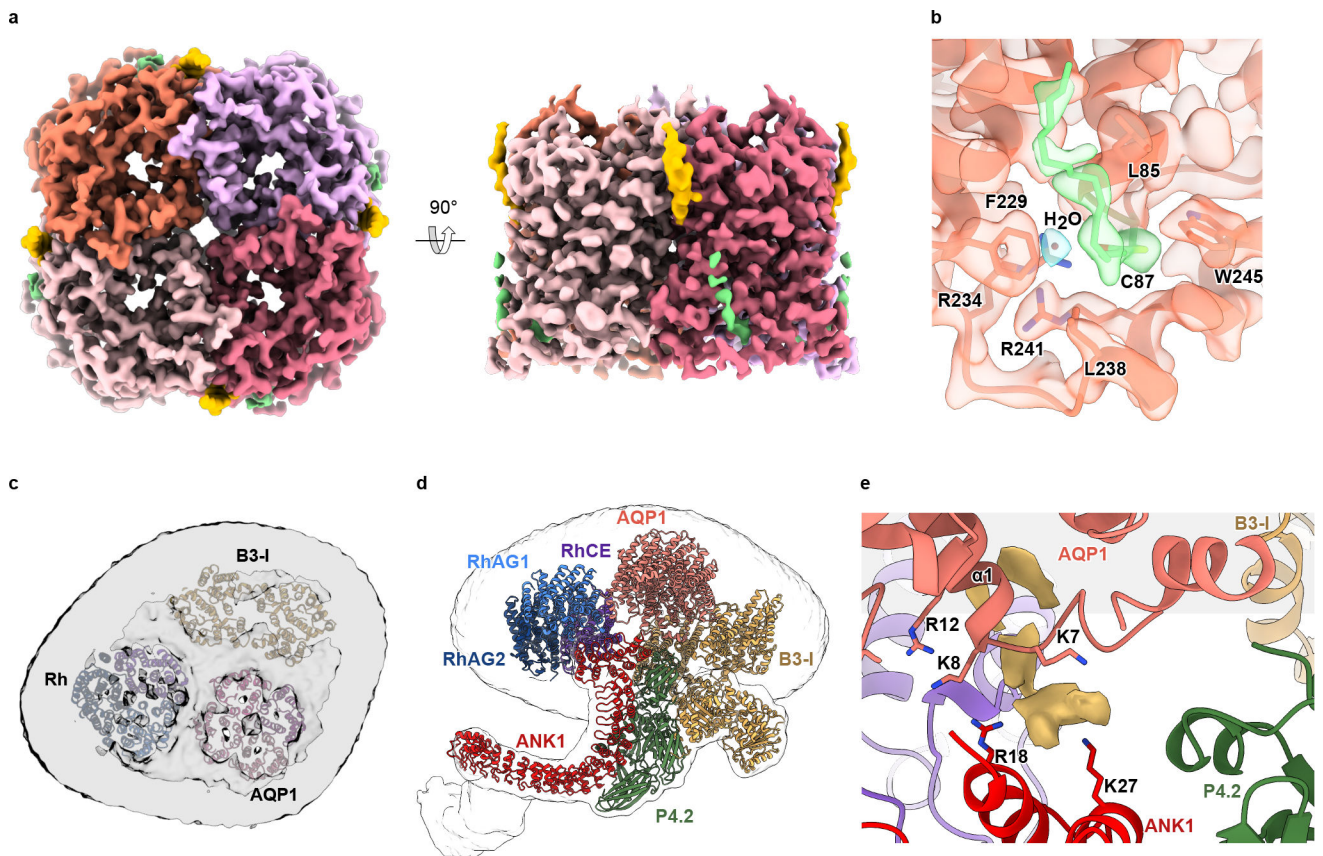


Fig. 4: Aquaporin is a component of the ankyrin-1 complex.

a, The 2.8 Å cryo-EM density map of the aquaporin in Class 2. Densities corresponding to the four subunits are colored in light orange, deep pink, medium purple and hot pink. **b**, Close up of AQP1 palmitoylation of Cys 87. **c**, Aquaporin-1 is present in Classes 2 and 5 (Extended Data Fig. 5). The cryo-EM density map of Class 2 shows inside the membrane the density and atomic models corresponding to aquaporin (salmon), Rh (purple, blue and light blue) and Band 3-I (orange)., **d**, The model of Class 2 shows that AQP1 (salmon color) is located at the mutual interface of protein 4.2 (green), ankyrin (red), RhCE (purple) and Band 3-I (orange). **e**, Close up of the interaction region between AQP1, protein 4.2 and ankyrin. The membrane is represented in gray. The key residues that mediate the interactions in the interfaces are shown as sticks.

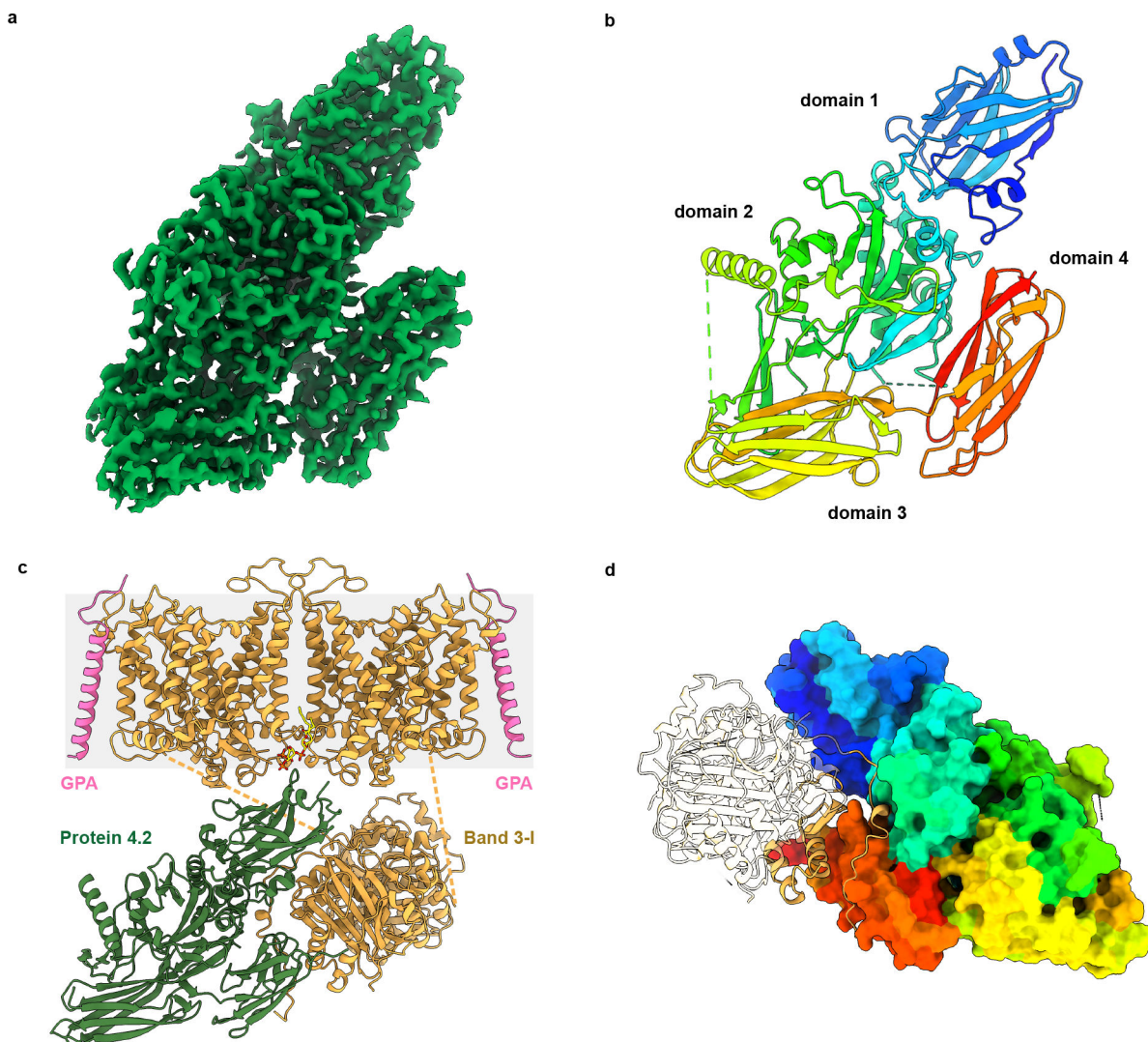


Fig. 5: (RhAG)₂(RhCE) trimer.

a, The structure of the (RhAG)₂(RhCE) trimer as viewed from the cytoplasm (right panel), and as viewed in the plane membrane (central and right panels). RhCE is colored in purple, RhAG1 in light blue and RhAG2 in dark blue. Two molecules of cholesterol (yellow) are bound to each RhAG. **b**, The 2.4 Å cryo-EM density map of the (RhAG)₂(RhCE) complex. Densities corresponding to RhCE, RhAG1 and RhAG2 and cholesterol are colored as in panel A. **c**, Refined atomic B-factors, averaged per residue. RhCE has higher B-factors than RhAG, likely indicating more flexibility/mobility. **d**, Cryo-EM density map of the Band 3-III-GPA, (RhAG)₂(RhCE) and GPB that mediates the interaction between the two. **e**, Close up of the interaction region between GPB and RhAG1. The sidechain of M71 is located in a hydrophobic pocket in the surface of RhAG1, and the key residues that mediate the interactions are shown as sticks.

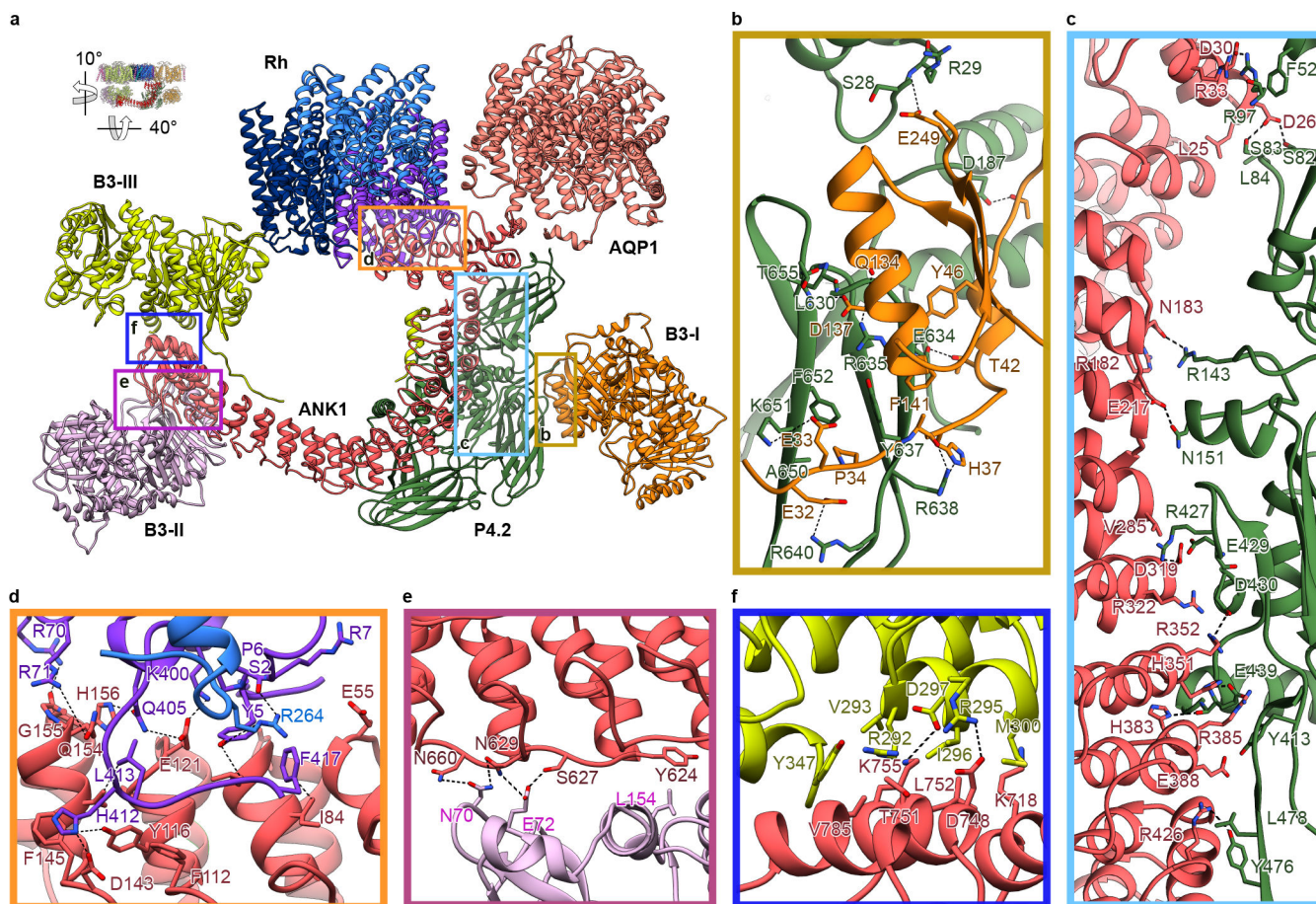


Fig. 6: Band 3 in complex with glycophorin A.

a, The structure of band 3 in complex with glycophorin A as viewed in the plane of the membrane, as viewed from the cytoplasm (central panel), and as viewed from inside the cell. Band 3 protomers are colored in aqua green and gray, glycophorin A in magenta, and molecules of cholesterol (yellow) PIP₂ (orange) and POPC (blue) are shown. Glycans are colored in green. **b**, The 2.3 Å cryo-EM density map of the band 3-glycophorin A complex. Density corresponding to band 3, glycophorin, cholesterol (bound to glycophorin) and PIP₂ are colored as in panel A. The three orientations of the map are the same as panel A. **c**, Close up of the interactions between band 3 (aqua green), glycophorin (magenta) and a cholesterol molecule (yellow). The key residues that mediate the interactions are shown as sticks. **d**, Close up of the band 3 transmembrane dimer interface. PIP₂ (orange) sits in the middle of the site. The key residues that mediate the interactions in the interfaces are shown as sticks. **e**, Cut through the TM of ankyrin-1 complex shows the position of glycophorin A bound to band 3 in the context of the complex. **f**, PIP₂ (orange) sits in the middle of the dimerization site of Band 3-I and close to the interaction site between Band 3-I and protein 4.2. The key residues that mediate the interactions in the interfaces and between Band 3-I TM and protein 4.2 are shown as sticks.

| Class2 | | | | | | | | | | | | | | | |
|---|--|---|--|---------------------------------|-----------------------------------|-----------------------------|--------------------------------------|---|---|--|------------------------------------|------------------------------------|---------------------|-----------------------------------|--------------|
| Band3-III cytosolic domain PDB 7V0Y EMD-26953 | Band3-I TM PDB 8CRQ EMD-26955 | Band3-II TM PDB 7V19 EMD-26954 | Band3-III TM PDB 8CRR EMD-26956 | Rh-GPB PDB 8CRQ EMD-26958 | Combined PDB 8CTE EMD-26988 | Rh PDB 8CSX EMD-26974 | Protein 4.2 PDB 8CSW EMD-26973 | Ankyrin N- term PDB 8CSV EMD-26972 | Band3-I cytosolic domain PDB 8CSV EMD-26975 | Band3-I TM PDB 8CT3 EMD-26979 | AQP1 (C1) PDB 8CT2 EMD-26978 | AQP1 (C4) PDB 7UZE EMD-26886 | Class4 EMD-26982 | Sub Tomo PDB 8CSL EMD-26965 | |
| 105,000x | 105,000x | 105,000x | 105,000x | 105,000x | 105,000x | 105,000x | 105,000x | 105,000x | 105,000x | 105,000x | 105,000x | 105,000x | 105,000x | 105,000x | 41,960x |
| 300 | 300 | 300 | 300 | 300 | 300 | 300 | 300 | 300 | 300 | 300 | 300 | 300 | 300 | 300 | 300 |
| 58 | 58 | 58 | 58 | 58 | 58 | 58 | 58 | 58 | 58 | 58 | 58 | 58 | 58 | 58 | 112 |
| -0.5 to -1.5 | -0.5 to -1.5 | -0.5 to -1.5 | -0.5 to -1.5 | -0.5 to -1.5 | -0.5 to -1.5 | -0.5 to -1.5 | -0.5 to -1.5 | -0.5 to -1.5 | -0.5 to -1.5 | -0.5 to -1.5 | -0.5 to -1.5 | -0.5 to -1.5 | -0.5 to -1.5 | -0.5 to -1.5 | -3.5 to -4.5 |
| 0.83 | 0.83 | 0.83 | 0.83 | 0.83 | 0.83 | 0.83 | 0.83 | 0.83 | 0.83 | 0.83 | 0.83 | 0.83 | 0.83 | 0.83 | 2.077 |
| CI | CI | CI | CI | CI | CI | CI | CI | CI | CI | CI | CI | C4 | CI | CI | CI |
| 14,926 | 14,926 | 14,926 | 14,926 | 14,926 | 14,926 | 14,926 | 14,926 | 14,926 | 14,926 | 14,926 | 14,926 | 14,926 | 14,926 | 14,926 | 100 |
| 14,464 | 14,464 | 14,464 | 14,464 | 14,464 | 14,464 | 14,464 | 14,464 | 14,464 | 14,464 | 14,464 | 14,464 | 14,464 | 14,464 | 14,464 | 100 |
| 710,437 | 710,437 | 710,437 | 710,437 | 710,437 | 710,437 | 710,437 | 710,437 | 710,437 | 710,437 | 710,437 | 710,437 | 710,437 | 710,437 | 710,437 | 60,029 |
| 126,197 | 85,645 | 44,624 | 96,966 | 22,953 | 145,645 | 145,645 | 145,645 | 145,645 | 145,645 | 71,451 | 145,645 | 108,425 | 51,283 | 1596 | |
| 2.95 | 3.14 | 3.33 | 2.96 | 3.0 | 4.05 | 2.40 | 2.47 | 2.73 | 2.71 | 3.32 | 3.04 | 2.42 | 4.1 | 24.6 | |
| 0.143 | 0.143 | 0.143 | 0.143 | 0.143 | 0.143 | 0.143 | 0.143 | 0.143 | 0.143 | 0.143 | 0.143 | 0.143 | 0.143 | 0.143 | 0.143 |
| 4,454 | 8,936 | 8,936 | 8,936 | 17,925 | 5,332 | 9,116 | 5,332 | 3,712 | 4,638 | 8,964 | 7,464 | 7,577 | - | 30,720 | |

| Class2 | | | | | | | | | | | | | | |
|---|-------------------------------------|--------------------------------------|---------------------------------------|---------------------------------|-----------------------------------|-----------------------------|--------------------------------------|---|---|-------------------------------------|------------------------------------|------------------------------------|---------------------|----------------------------------|
| Band3-III cytosolic domain PDB 7V0Y EMD-26953 | Band3-I TM PDB 8CRQ EMD-26955 | Band3-II TM PDB 7V19 EMD-26954 | Band3-III TM PDB 8CRR EMD-26956 | Rh-GPB PDB 8CRO EMD-26958 | Combined PDB 8CTE EMD-26988 | Rh PDB 8CSX EMD-26974 | Protein 4.2 PDB 8CSW EMD-26973 | Ankyrin N-term PDB 8CSV EMD-26972 | Band3-I cytosolic domain PDB 8CSY EMD-26975 | Band3-I TM PDB 8CT3 EMD-26979 | AQP1 (C1) PDB 8CT2 EMD-26978 | AQP1 (C4) PDB 7UZE EMD-26886 | Class4 EMD-26982 | SubTomo PDB 8CSL EMD-26965 |
| 558 | 1,114 | 1,114 | 1,114 | 2,305 | 657 | 1,158 | 483 | 584 | 1,114 | 988 | 988 | 988 | - | 7,677 |
| 5 | 5 | 4 | 5 | 5 | 5 | 5 | 3 | 5 | 4 | 4 | 4 | 3 | - | NA |
| 5 | 1 | 2 | 2 | 2 | 2 | 2 | 2 | 3 | 0 | 2 | 2 | 1 | - | NA |
| 98 | 98 | 98 | 98 | 98 | 99 | 98 | 97 | 98 | 99 | 97 | 97 | 97 | - | NA |
| 2 | 2 | 2 | 1 | 1 | 1 | 2 | 3 | 2 | 1 | 3 | 3 | 3 | - | NA |
| 0 | 0 | 0 | 0 | 0 | 0 | 0 | 0 | 0 | 0 | 0 | 0 | 0 | - | NA |